



Application of Landsat imagery for the investigation of wave breaking

A.A. Kubryakov^{*}, V.N. Kudryavtsev, S.V. Stanichny

Federal State Budget Scientific Institution, "Marine Hydrophysical Institute of RAS", Sevastopol, Russia

ARTICLE INFO

Keywords:

Landsat-8 imagery
Whitecap coverage retrieval algorithm
Whitecaps vs. wind
Dissipation proxy
Internal waves
Bottom topography
Ocean fronts
Atmospheric stability

ABSTRACT

An algorithm for retrieving the fraction of the sea surface covered by whitecaps (W) from Landsat-8 satellite optical reflectance measurements in the near-infrared channel is described. The distribution of W derived from approximately 100 Landsat-8 scenes was compared with quasi-synchronous scatterometer measurements of wind speed (u_{10}), which allowed us to obtain the $W(u_{10})$ relation for large whitecaps from high-resolution satellite optical measurements. Further, we demonstrate the impact of various phenomena, including- internal waves, river plumes, bottom topography, atmospheric stability, ocean fronts, and mesoscale currents on whitecap coverage and its spatial variation in different areas of the ocean. These data are analysed using theoretical models, suggesting that whitecap coverage is a proxy of wave energy dissipation and reflects disturbances in the wind-wave energy balance caused by wave-current interactions and variable wind forcing due to changes in atmospheric stratification over ocean temperature fronts and the movement of wind-waves by surface currents relative to the atmospheric boundary layer.

1. Introduction

Whitecaps are a visualisation of the wind-wave breaking process. Entrainment of the air into the breaking crest generates a large number of bubbles, which strongly reflect light, making them visible. Wave breaking dissipates wave energy and thus plays a key role in the energy budget of wind-waves (Phillips, 1985; Kraan et al., 1996; Banner et al., 2000; Thomson et al., 2009; Babanin, 2009). Breaking waves drive mixing below the surface, enhancing the transfer of energy, momentum, heat, and gas (Melville et al., 2005), and can noticeably increase turbulence in the upper ocean layer (Mellor and Blumberg, 2004; Ardhuin and Jenkins, 2006; Kudryavtsev et al., 2008; Toffoli et al., 2012; D'Asaro, 2014; Wu et al., 2015)

The formation of whitecaps is related to wave dissipation and, therefore, the spatio-temporal variability of whitecaps reflects the evolution of the wave energy balance. The main source of wave energy is wind, which dominates whitecap coverage via energy dissipation. After Monahan (1971), the fraction of the sea surface covered by whitecaps, W (whitecaps fraction hereinafter), is usually parameterised as a power function of wind speed at 10 m u_{10} :

$$W = a^*(u_{10} - u_0)^n$$

where u_0 is the minimum wind speed when whitecaps appear (u_0 ranges

from 0 to 5 m/s), and a and n are empirical coefficients. Experimental estimates of the wind exponent can vary significantly from 1 to 5 (see reviews by Anguelova and Webster, 2006, and Brumer et al., 2017).

Such large scatter of n is related to different methods used to detect whitecaps (e.g. choice of the threshold level for identification) and the influence of various processes affecting their formation, e.g. atmospheric stratification (Monahan and Muircheartaigh, 1980; Monahan and O'Muircheartaigh, 1986; Anguelova and Webster, 2006; De Leeuw et al., 2011; Salisbury et al., 2013), surface tension, which is dependent on water temperature, salinity, and surfactants (Monahan and O'Muircheartaigh, 1986; Wu, 1988; Stramska and Petelski, 2003; Salisbury et al., 2013; Callaghan et al., 2014; Hansen et al., 2016), wave-current interaction (Dulov and Kudryavtsev, 1990; Dulov et al., 1986; Kudryavtsev et al., 1995; Kraan et al., 1996; Melville et al., 2005; Romero et al., 2017), the wave age of wind seas, and the presence of swell (Donelan et al., 1993; Kraan et al., 1996; Dulov et al., 2002; Gemmrich et al., 2008; Callaghan et al., 2008; Thomson et al., 2009; Kleiss and Melville, 2010; Goddijn-Murphy et al., 2011; Plant, 2012; Sutherland and Melville, 2013; Salisbury et al., 2013; Brumer et al., 2017).

Wave-current interaction can significantly modify the energy balance of wind-waves, thus leading to spatio-temporal variability in energy dissipation and, consequently, the whitecap fraction (Kudryavtsev et al., 1995; Kraan et al., 1996; Melville et al., 2005; Romero et al.,

^{*} Corresponding author.

E-mail addresses: arskubr@gmail.com, arskubr@ya.ru (A.A. Kubryakov).

2017). The effect of atmospheric boundary layer transformation over sea surface temperature (SST) variations related to sub-meso-, meso-, and large-scale currents provides an additional contribution to whitecap variability in ocean frontal zones (Dulov and Kudryavtsev, 1990; Dulov et al., 1991). Particularly, Thomson et al. (2014) and Zippel et al. (Zippel and Thomson, 2017; Zippel et al., 2018) showed that intensification of wave breaking is observed on river plume fronts, which promotes the mixing of plumes with the surrounding waters. Measurements by Dulov et al. (1986) and Thorpe et al. (1987) also revealed the significant modulations of W caused by the currents induced by internal waves on the ocean surface.

The spectral properties of whitecaps in the visible and infrared bands have been investigated in laboratory and field experiments (Whitlock et al., 1982; Koepke, 1984, 1986; Frouin et al., 1996; Moore et al., 2000). In optical and near-infrared bands, out of the sun glitter areas, whitecaps are significantly brighter than the ocean surface because of the strong reflectance of the incident radiance due to the conglomeration of bubbles in the whitecaps. For example, the brightness of whitecaps at $\lambda = 800$ nm is $\sim 55\%$ that is ten-fold higher than the reflectance of “pure” seawater, even during strong winds (0–3%) (Koepke, 1985).

Owing to such high reflectance, whitecap detection using video, photography, and visual inspection from observing platforms based on the threshold level is routinely used (Cox and Munk, 1954; Monahan, 1971; Ross and Cardone, 1974; Monahan and Muircheartaigh, 1980; Monahan and O’Muircheartaigh, 1986; Moore et al., 2000; Bondur and Sharkov, 1982; Stramska and Petelski, 2003; Mironov and Dulov, 2007; Callaghan and White, 2009; Goddijn-Murphy et al., 2011; Kleiss and Melville, 2010; Randolph et al., 2016). Such observations have high space and time resolution but often lack the coverage needed to better understand whitecap properties and their distribution at the scales corresponding to ocean sub- and mesoscale processes.

In the 1970s, an idea to use high-resolution satellite optical imagery to observe the whitecaps from space had been suggested (e.g. Maul and Gordon, 1975; Gordon and Jacobs, 1977; Koepke, 1985). Later, this approach was elaborated and implemented; in particular, Zhang et al. (2015) reported the data on spatial variability of whitecap coverage induced by submarine sand waves near the Taiwan Banks derived from Cartosat-1 satellite measurements. More recently, high-resolution satellite optical datasets have become freely available. Of these, the Operational Land Imager (OLI) sensor mounted on the Landsat-8 satellite is widely used. Because of the significantly enhanced signal-to-noise ratio, Landsat-8 detects relatively small variations in ocean brightness, which opens up new opportunities for investigating ocean processes (Schott et al., 2016).

Here, we demonstrate the capabilities of Landsat-8 imagery for observing and quantifying whitecap variability caused by different atmospheric and ocean processes including wind field and atmospheric stratification, mesoscale currents, river plumes, internal waves, and bathymetry features. The remainder of the paper is organised as follows. First, we demonstrate the possibility of using Landsat to observe the spatial variability of wave breaking (Section 3.1) and suggest an algorithm for the estimation of the whitecap fraction in a pixel from Landsat imagery based on reflectance (Section 3.2). We then use more than 100 quasi-synchronous images of Landsat-8 reflectance and maps of Ascatt scatterometry winds to compute the dependence of whitecaps on the wind velocity u_{10} (Section 4.1) and demonstrate the impact of wind variations due to atmospheric waves on whitecap coverage (Section 4.2). In Section 5, we demonstrate and investigate the response of whitecap coverage to different ocean phenomena, namely bottom topography (Section 5.1), internal waves (Section 5.2), river plumes (Section 5.3), frontal features (Section 5.4), and “large-scale” ocean surface currents (Section 5.5). Conclusions are provided in Section 6.

2. Data

2.1. Landsat data

This study is based on Landsat-8 data for the period 2013–2017. Landsat-8 has a ground track repeat cycle of 16 days with an equatorial crossing time at 10:00 a.m. It contains two main sensors—the operational land imager (OLI) and the thermal infrared sensor (TIRS). The OLI is a push broom scanner that measures nine channels in optical, near-infrared (NIR), and shortwave infrared (SWIR) bands. It has a swath width of 185 km, eight channels at 30 m, and one panchromatic channel with a 15-m spatial resolution (Table 1). In this study, to identify whitecaps and mask clouds and land, we used bands 5, 6, and 9 centred on 865, 1620, and 1375 nm, respectively. One of the important advancements of Landsat-8 sensors compared with previous Landsat series is a significantly improved signal-to-noise ratio, which is enhanced by a factor of 100 (Schott et al., 2016). The TIRS works in two long-wavelength infrared bands centred at 11 μm and 12 μm with a 100-m spatial resolution (Reuter et al., 2015).

Thermal and optical measurements provide simultaneous information about the optical properties of the surface (e.g. whitecap coverage, see Section 3, 4) and the SST features associated with, for example, oceanic fronts and dynamics. The Level 1 data used in this study were taken from the United States Geological Survey (USGS) Global Visualisation Viewer (<http://glovis.usgs.gov/>) and the Amazon S3 web service (<http://landsat-pds.s3.amazonaws.com>).

Top-of-atmosphere (TOA) ocean radiances and planetary reflectance (ρ) were computed from the digital numbers (DN) of the downloaded files using $L = M1 \times DN + A1$; $\rho_l = M2 \times DN + A2$, where constants $M1$, $M2$, $A1$, and $A2$ are rescaling coefficients included in the product metadata file (MTL file). TOA reflectance (ρ) was computed by normalising TOA values to the band averaged irradiance:

$$\rho = \frac{\rho_l}{\cos(\theta_z)}$$

where θ_z is the average solar zenith angle average for the scene.

2.2. Other data

For the analysis of wind characteristics, we used the MetOp-A ASCAT Level 2 Ocean Surface Wind Vectors Optimised for Coastal Ocean Product (KNMI, 2010; <https://podaac.jpl.nasa.gov/dataset/ASCATA-L2-Coastal>). This dataset contains operational near-real-time Level 2 coastal ocean surface wind vector retrievals from the Advanced Scatterometer (ASCAT) on the MetOp-A and MetOp-B satellites with a 12.5-km sampling resolution. This product is provided by the European Organisation for the Exploitation of Meteorological Satellites (EUMETSAT) of the Ocean and Sea Ice Satellite Application Facility (OSI SAF) administered by the Royal Netherlands Meteorological Institute (KNMI). We also used wind velocity data 10 m above the sea surface obtained from the Modern Era Retrospective Analysis for Research and Applications (MERRA) reanalysis (Rienecker et al., 2011) with a spatial resolution of $1/2^\circ \times 2/3^\circ$. MERRA is the National Aeronautics and Space Administration (NASA) reanalysis dataset for the satellite era in which a major new version of the Goddard Earth Observing System Data Assimilation System Version 5 (GEOS-5) was used. Data were downloaded from <http://goldsmr2.sci.gsfc.nasa.gov/>.

The mapped geostrophic velocities obtained from the combined measurements of several altimetric satellites were used for the surface current analysis. The altimeter products were produced by Ssalto/Duacs and distributed by Aviso with support from the French National Centre for Space Studies (CNES) (<http://www.aviso.altimetry.fr/duacs/>). The spatial resolution of the product is $1/4^\circ$ and the temporal resolution is 1 day. Bathymetry data from the Gebco dataset with 30-s resolution (Becker et al., 2009) were also used in Section 4.1.

3. Methods

3.1. Visual inspection of whitecaps in Landsat data

In the NIR and SWIR channels, open ocean water acts almost like a black body; water absorption is close to 1 and the underwater-leaving radiance is low. Whitecaps significantly increase the reflectance of the

sea surface; the reflectance of whitecaps at a wavelength of 800 nm is approximately 0.55, which is more than 10-times higher than that of pure water (Koepke, 1984; Whitlock et al., 1982; Frouin et al., 1996; Moore et al., 2000; Kokhanovsky, 2004). Although the area of an individual whitecap is often smaller than the pixel size (30×30 m), its high brightness makes a noticeable contribution to the pixel reflectance. Thus, a field of whitecaps in NIR and SWIR band images should be

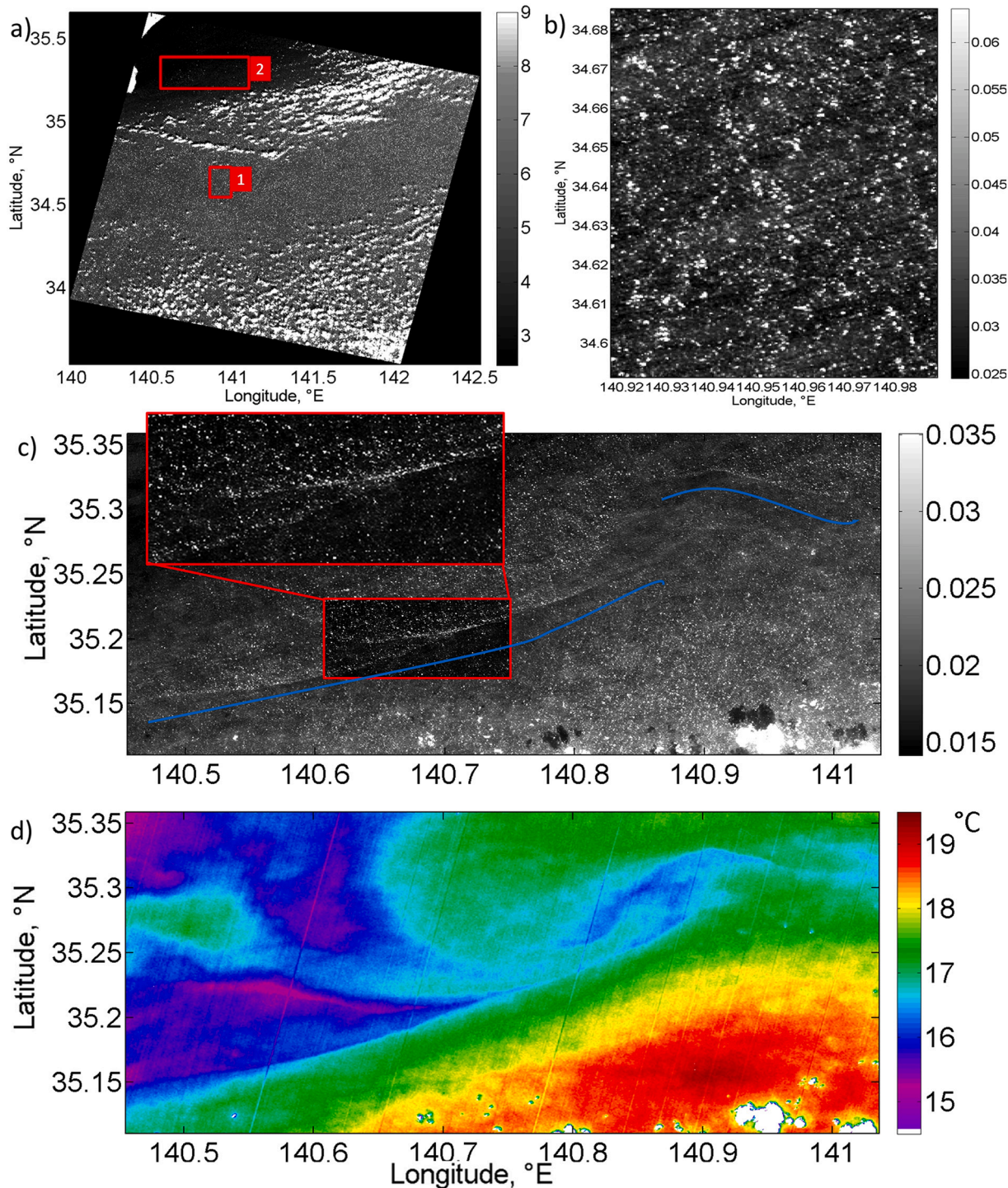


Fig. 1. a) Landsat-8 brightness in channel 5 (0.845–885 nm) in the vicinity of Kuroshio, Pacific ocean on 01 December 2014. Red boxes show the location of fragments #1 and #2 shown in plots 1b and 1c. b) Fragment #1 in Fig. 1a showing the whitecaps manifestations in Landsat-8 reflectance data. c) Fragment #2 in Fig. 1a showing the features of the spatial distribution of the whitecaps in the vicinity of the thermal fronts (underlined by blue lines) d) The sea surface temperature reconstructed from Landsat-8 thermal channel 11. (For interpretation of the references to colour in this figure legend, the reader is referred to the web version of this article.)

exposed as an ensemble of bright pixels randomly distributed over the “dark” surface (see examples in Figs. 1–2). In this section, we demonstrate two examples of Landsat images with the manifestation of different ocean phenomena in the fields of visually observed whitecaps. The method of detection and quantification of whitecaps is considered in the Section 3.2.

Fig. 1a shows a Landsat-8 scene during an intense storm in the vicinity of the Kuroshio Current with wind velocities exceeding 22 m/s. Randomly distributed white spots of different sizes (i.e., individual wave-breaking events) are visible in the enlargement (Fig. 1b) marked by box#1 in Fig. 1a. Fig. 1c, which corresponding to box#2 in Fig. 1a, demonstrates two distinct linear zones of enhanced whitecapping. Referring to the Landsat thermal image in Fig. 1d, these zones of enhanced wave breaking are associated with SST fronts, which suggests that wave-breaking anomalies trace the ocean frontal features. This is consistent with previously reported findings (Kudryavtsev et al., 1995; Melville et al., 2005; Romero et al., 2017; Kudryavtsev et al., 2012).

Fig. 2 demonstrates the manifestation of wave breaking in the Landsat-8 reflectance image during an intense katabatic jet wind in the Mediterranean Sea (the so-called Mistral winds) on 31 December 2014. According to the Ascat data, the wind speed during this event reached 17 m/s. Fig. 2b demonstrates that the size of the whitecaps and whitecap spacing noticeably increased in the offshore direction. This is presumably related to the wind-wave development with fetch (Gemrich et al., 2008; Kleiss and Melville, 2010). A number of linear zones of enhanced whitecaps are visible in the mistral area, shown as red lines in Fig. 2a. These are possibly related to wave-current interactions leading to the enhancement/suppression of wave energy and, thus, wave breaking in the vicinity of the surface current gradients. Detailed inspection of waves in the vicinity of one of the current fronts in Fig. 2c reveals the wave trains travelling in an “anomalous” southwest direction, while ambient waves travel in the Mistral direction. The location of these “anomalous” waves is probably linked to the velocity gradient on the front. Waves travelling along the front are highlighted by whitecap enhancement and may be treated as surface waves trapped by the current, similar to those observed in ship experiments by Kudryavtsev et al. (1995) and, more recently, using Sentinel-2 imagery by Kudryavtsev

et al. (2017) and Quilfen et al. (2018).

3.2. Whitecap fraction retrieval

A total of 209 Landsat-8 scenes were used to analyse whitecap variability in different areas of the world’s oceans. To identify the whitecaps from the Landsat images, we detected and counted the intense brightness maxima in each scene using an algorithm consisting of the following steps:

Step 1: To avoid contamination by sunlight spots, we considered only those scenes with azimuthal angles from 30° to 70°, which were out of the sun glint centre. We also excluded data with low solar angles at high latitudes. Visual inspection revealed that under these conditions, the noise of reflectance measurements increases, which impacts the whitecap identification.

Step 2: The land-affected and cloud-affected pixels were excluded from the images using reflectance in bands 5, 6, and 9, and visually defined thresholds. The SWIR measurements (band 6) were used to distinguish the water area, which is significantly darker than the land and thin clouds due to high water absorption. A threshold of $R(6) = 0.04$ was chosen for this task. This filtration also excludes pixels with artificially bright objects such as ships and platforms. Band 9 of the Landsat satellite, which corresponds to the absorption line for water vapour, was included in the OLI sensor for the filtration of thin cirrus clouds. We use a threshold value of $R(9) = 0.003$ to filter cirrus clouds from the images. We also excluded the five nearest pixels to land and clouds to remove possible errors related to cloud shadows or bottom reflectance.

Step 3: A portion of “whitecap-affected” pixels is covered by foam or actively breaking waves and the remaining portion is clear water. The fraction of the whitecaps in the “whitecap-affected” pixels was further calculated based on reflectance, using a similar method as suggested by Koepke (1986) and Xu et al. (2015). The reflectance of the surface without whitecaps in the NIR channels at the satellite orbit depends on atmospheric reflectance (R_a), atmospheric transmittance (t), water optical properties R_{turb} (turbidity), and the bidirectional Fresnel reflection of the sun and skylight by wave slopes (R_f). R_f is a function of wind speed and scan geometry (Koepke, 1986). The reflectance of the “whitecap-

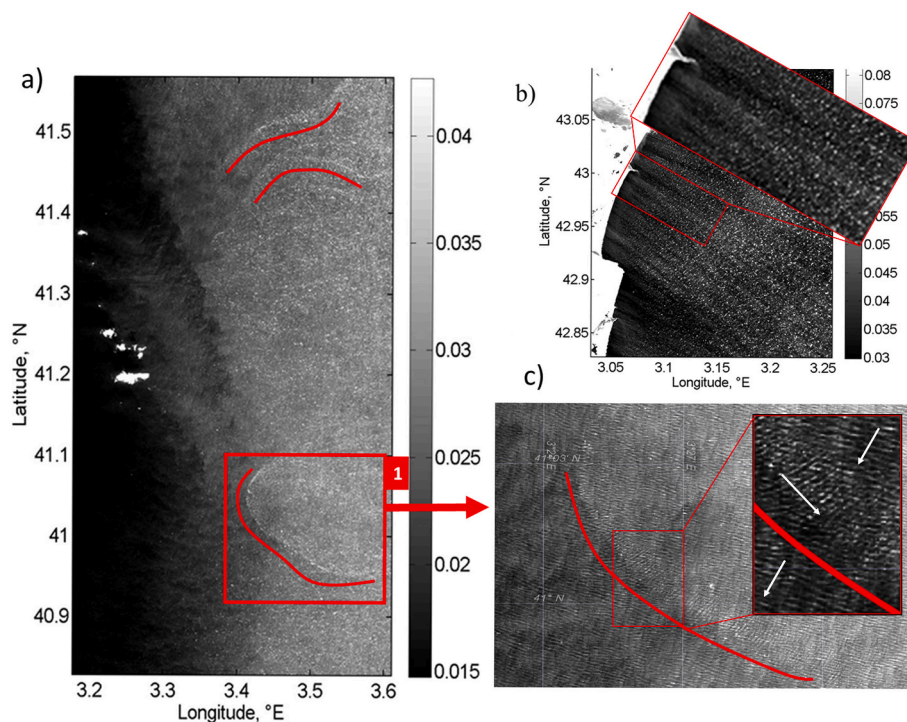


Fig. 2. a) Landsat-8 brightness at 865 nm in the Gulf of Lion, Mediterranean Sea, during the development of the Mistral winds at 31 December 2014 (red lines underline increased whitecaps zones); b) Fragment of the Landsat scene showing the development of katabatic winds and increase of wave breakers length; c) Zoomed Landsat-8 scene, where trapping of surface waves by front and sharp change of their direction is observed; (For interpretation of the references to colour in this figure legend, the reader is referred to the web version of this article.)

affected” points (R) and the reflectance of the unaffected pixel (clear water, R_c) can be expressed as:

$$\begin{aligned} R &= R_a + t \times ((R_{turb} + R_f) * (1 - W) + W * R_{wc}) \\ R_c &= R_a + t \times (R_{turb} + R_f) \end{aligned} \quad (1)$$

where R_{wc} is the estimated reflectance of active breakers (equal to 0.55; Koepke, 1984; Frouin et al., 1996), and W is the area fraction covered by whitecaps. Atmospheric transmittance (t) in the NIR region is approximately 0.7–0.8 (Selby, 1978), with a value of 0.75 applied here.

Step 4: The reflectance of “whitecap-affected” pixels is significantly higher than the reflectance of clear water, visible as bright outliers over the dark surface (see Figs. 1 and 2). To identify these outliers, we high-passed reflectance by applying Wiener-2d adaptive noise-removal filtering (Lim, 1990) based on the computation standard deviation against the local mean. Following a series of tests, we applied a filter with a window size of 20×20 pixels (600×600 m). This allowed us to exclude large-scale background variation in the reflectance field and detail only extreme values. Positive extreme values correspond to

whitecaps and are further used in Step 5. Negative extreme values are mostly related to cloud shadows and are excluded from the analysis.

Further, to define the reflectance of clear water (R_c) we use the “darkest” point method. We assumed that background optical and atmospheric properties (R_c) are relatively uniform across scales of 5 km. At these spatial scales, out of the direct influence of sun glint, the impact of the change in the observation angle on total reflectance can also be assumed to be small.

To determine the reflectance of clear water, we computed minimal values of the filtered reflectance in boxes with a size of 150×150 pixels (4.5×4.5 km) and obtained the spatial distribution of R_{min} . Then, R_{min} was filtered by median filtration with a size of 3×3 pixels to exclude possible remaining outliers. These outliers are mostly related to cloud shadows, which may still be present after Step 3. The computed distribution of R_{min} is further used as R_c .

An example of the analysis of the computed distribution of R_{min} for the scene taken in the Mediterranean Sea on 31 December 2014 (see Fig. 2) in comparison to the quasi-synchronous wind field obtained by

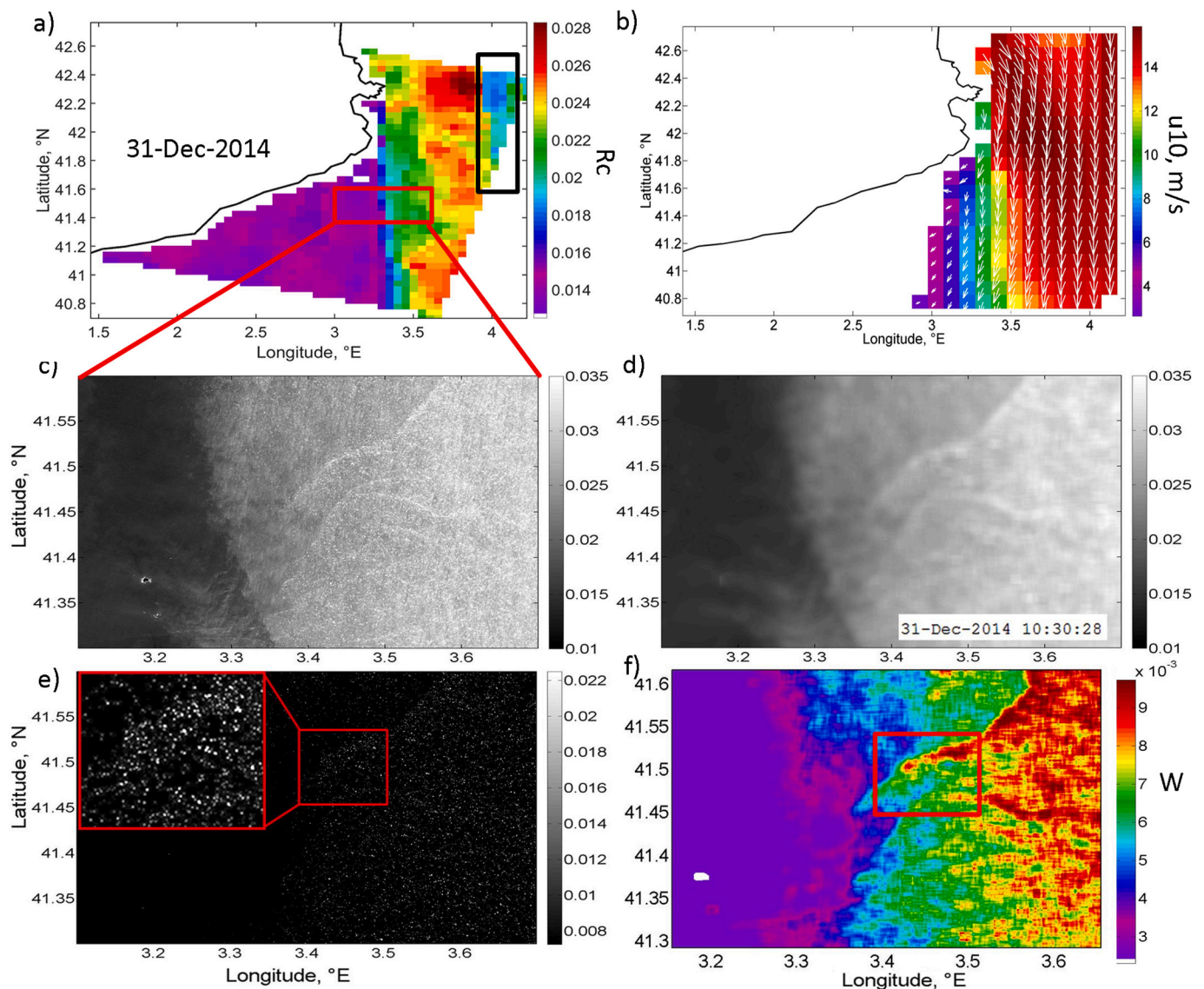


Fig. 3. Illustration of the algorithm of the calculation of whitecap fraction from Landsat-8 for 31 December 2014 in the Gulf of Lion: a) R_{min} calculated as an estimate of background reflectance of clear water. Black rectangle shows the area with decreased R_{min} caused by the impact of the cloud shadows. b) Wind velocity (m/s) from quasi-synchronous Ascet measurements; c) Reflectance at channel 5 (0.845–885 nm) in the zoomed part of the scene in Fig. 3a. d) Low-passed reflectance after Wiener-2d filtering; e) High-passed reflectance after Wiener-2d filtering; f) Whitecaps fraction calculated from Landsat data and smoothed by 10×10 moving average filter.

Ascat is shown in Fig. 3a. The spatial variability of R_{\min} mainly reflects the variation in mean surface slope (Fresnel reflection) caused by wind variability (see the Ascat wind map in Fig. 3b). According to Cox and Munk (1954), Fresnel reflection can be represented as a linear function of wind. Fig. 3a demonstrates that in this example, R_f rises to 0.01 when the wind changes at 10 m/s. In the eastern storm area where the wind velocity is 15 m/s, R_{\min} reaches 0.024. To the west of 3.2°E, where the wind velocity is less than 4–5 m/s, R_{\min} is approximately 0.0013. This gives estimates of the atmospheric contribution, R_a , which is roughly equal to the reflectance of the calm waters ($R_a = 0.01$).

Step 5. The whitecaps-affected pixels are the positive extreme values of reflectance. After Weiner filtration in Step 3, the pixels with filtered reflectance values higher than the chosen threshold equal ($cf = 0.002$) are taken as “whitecap-affected” pixels with reflectance R_w . We choose this threshold empirically on the basis of manual comparison of the results with the visual analysis of more than 100 Landsat-8 scenes. The effective reflectance of the foam in the NIR band is approximately 0.22 and the reflectance of active breakers is approximately 0.55 (Koepeke, 1984; Frouin et al., 1996). Therefore, the chosen threshold only retains those pixels with a foam ratio greater than 0.002/0.22–1% or active breakers (whitecaps) with a ratio of more than 0.3%. This corresponds to $0.01 \times 900 \text{ m}^2 = 9 \text{ m}^2$ of a foam-covered area in a pixel or approximately 3 m^2 covered by active breakers where $R_{wc} = 0.55$. As this method is based on a fixed threshold of average pixel reflectance ($30 \times 30 \text{ m}$), it does not allow the differentiation of active breakers and foam (or stages A and B of wave breaking).

Figs. 3c–e show the raw, low-passed, and high-passed reflectance for the Landsat-8 scene given in Fig. 3a. Individual whitecap affected pixels are bright points, which are clearly distinguished in the enlargement in Fig. 3c.

From Eq. (1), the fraction of the whitecaps, W , for the point with reflectance R can be defined as:

$$W = (R - R_c) / (R_{wc} - R_{turb} - R_t)$$

As demonstrated in Fig. 3a, $R_{wc} = 0.55$ is significantly higher than R_c and can be written as:

$$W = (R - R_c) / (tR_{wc}) \quad (2)$$

This formula is used to calculate the spatial distribution of the total whitecap fraction (including both foam and active wave breakers) for the Landsat scenes at the original resolution. The whitecap fraction is calculated only in the “whitecap-affected” pixels as defined in Step 5. For other points, W is set to zero. Therefore, our approach only included a fraction of the relatively large whitecaps on the ocean surface. An example of the calculated whitecap fraction maps is given in Fig. 3f, in which the whitecap fraction was low-passed using a 10×10 pixel running-average filter. The distribution of whitecaps in Fig. 3f is significantly non-uniform, which is related to both wind changes and dynamical effects, as demonstrated in Fig. 2c and Fig. 3b.

The proposed method for the detection of whitecap coverage has several possible sources of errors that should be acknowledged. First, cloud shadows can still affect the distribution of R_{\min} (or R_c) after several filters are used. In the example given in Fig. 3, this error causes a decrease in R_{\min} in the northwest part of the scene (the black rectangle in Fig. 3a) of approximately 0.005–0.01. The reflectance of the whitecap-affected pixels in this area was 0.03 on average. Thus, according to Eq. (2), W in the pixels affected by cloud shadows may be 15–30% higher due to the uncertainties in R_{\min} . A more robust algorithm for the detection of cloud shadows is, therefore, needed to fully exclude their impact on optical reflectance. The spatial variability of turbidity in coastal waters, especially during strong winds, and variability in atmospheric reflectance (e.g. due to terrestrial dust or cyanobacterial blooms) can be high even at scales of less than 5 km. These effects were significant in the coastal zone of approximately 5% of the analysed scenes, which were further excluded from the analysis. At high latitudes,

melting ice or small-scale ice floes can make a large contribution to reflectance and may be incorrectly detected as whitecaps. Finally, atmospheric transmittance may vary due to the presence of strong absorptive aerosols, which broadly varied between 0.7 and 0.8, giving an uncertainty of approximately 15%.

4. Whitecap coverage and wind speed

4.1. Background dependence

First, we checked the capability of the proposed method to reproduce the known dependence of whitecap coverage on wind speed. As a reference wind speed, we used the Ascat-A/B scatterometer wind product coinciding with Landsat data within ± 1.5 h. Several examples of whitecap coverage, wind speed fields, and corresponding scatterplots are shown in Fig. 4. For comparison, the whitecap fields were binned on a $1/8^\circ$ grid coinciding with the wind data grid for the scatterplots.

The first example (Fig. 4a, left-hand panel) demonstrates the ability of the method to describe the spatial variability of whitecaps associated with wind. In this case, a “wind jet” of $u_{10} = 12\text{--}15$ m/s blows westward along the South African coast (Fig. 4a, centre panel) and generates an intense wave-breaking field visible in the southern part of the Landsat-8 scene in the vicinity of the Cape of Good Hope. To the north (latitudes $>34.5^\circ\text{S}$) the wind field decelerates (< 6 m/s), leading to the disappearance of the whitecaps in the Landsat-8 image. Another feature of the spatial variability of W seen from the Landsat data is the increased wave breaking (indicated by the red oval in Fig. 4a) that extends from the coast from $\sim 34.4^\circ\text{S}$, 19°E . This is probably associated with the small-scale coastal jet, which is not represented in the wind data. Although the scatterometer winds are of the highest possible resolution, this is still not sufficient to capture small-scale wind variability, which is resolved in the maps of the Landsat whitecap fraction. Fig. 4a (right-hand panel) demonstrates the dependence of $W(u_{10})$ in this scene, which shows a robust correlation of 0.8, and can be approximated by the cubic function in agreement with the existing literature (e.g. Monahan, 1971).

The example in Fig. 4b demonstrates two offshore wind jets (with $u_{10} > 15$ m/s) associated with the Mistral event in the Gulf of Lion. The intense wave-breaking field generated by the Mistral along with the absence of whitecap events between the two jets in the low-wind area are well captured on the Landsat-8 image using the proposed algorithm (Fig. 4b).

A more complex spatial distribution of whitecap coverage was observed in the vicinity of Cape Nao, Spain (Fig. 4c), where up to four local zones of enhanced wave breaking are revealed. The position of these zones is correlated with the local features of the wind field caused by mountain shadowing at Cape Nao. Fig. 4c (right-hand panel) provides a quantitative relationship between the observed wind speeds and derived whitecap coverage.

Lastly, Fig. 4d demonstrates the ability of Landsat-8 to map whitecap coverage in high latitudes. A strong wind speed area along the westward side of Greenland is observed in the Ascat data, and the whitecap field broadly corresponds to the observed wind field. However, some remarkable differences can be seen, attributed to the “small-scale” structure of the wind field, which is not resolved by the scatterometer but is detected in the whitecap field. The second important reason for the strong spatial variability of W is the dynamic effect that can significantly alter the wave-breaking patterns (see Section 4). In addition, the presence of small areas of sea ice can complicate the identification of whitecaps at high latitudes. Nevertheless, the differences in this example between u_{10} and W are quite robust (Fig. 4d, right-hand panel).

In total, 117 quasi-synchronous Landsat-8 scenes and Ascat wind data were selected for the analysis, which correspond to more than 40,000 quasi-synchronous measurements of wind velocity and the whitecap fraction averaged in $1/8^\circ$ bins. All the collected W data are shown in Fig. 5a as a function of wind speed, where colors show a number of data points in the box, and the black curve shows the average

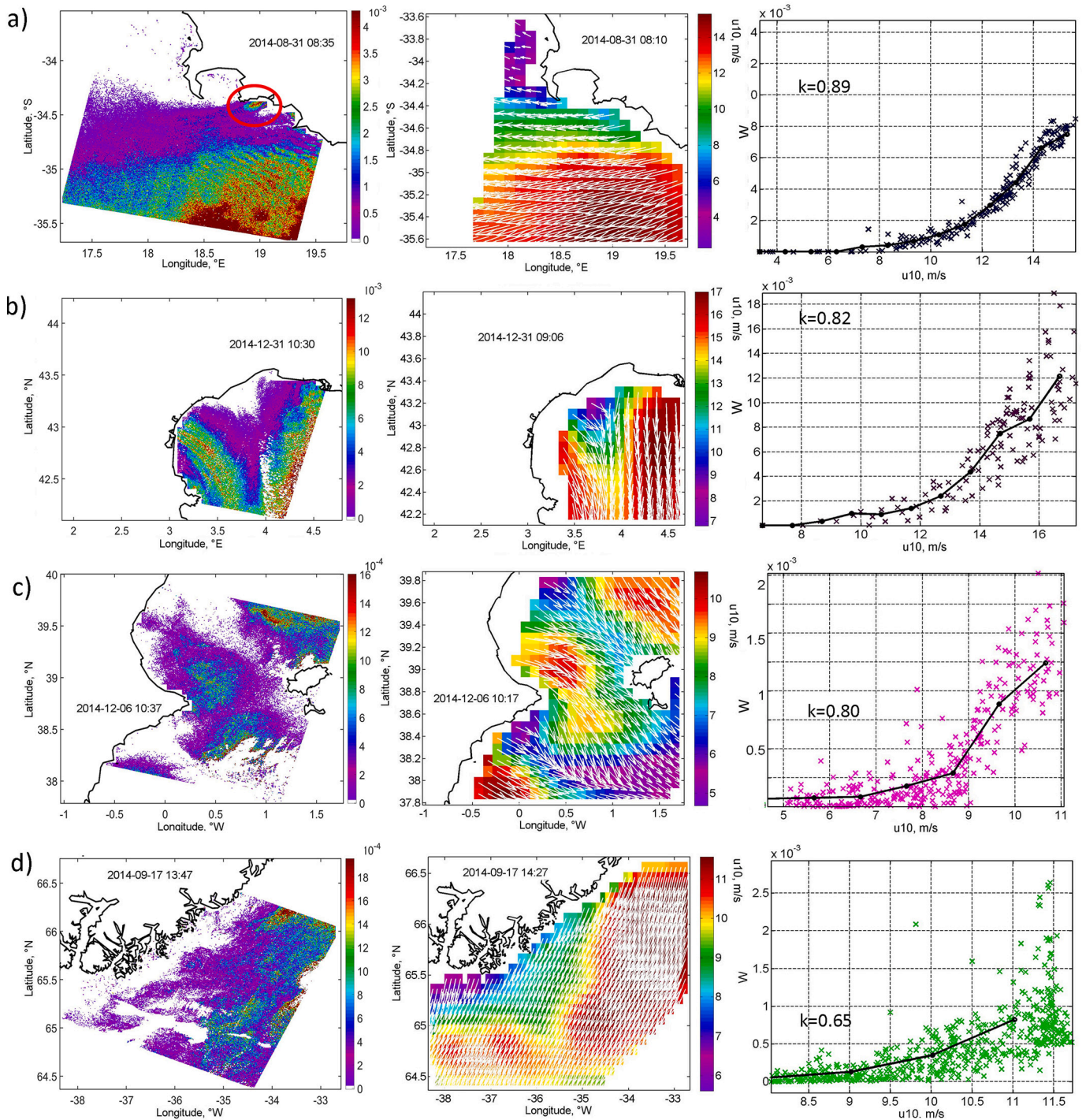


Fig. 4. (Left column) Examples of the derived whitecaps fraction, W ; (mid column) Ascac-wind fields, u_{10} ; (right column) dependence of W on u_{10} for four Landsat-8 scenes (a) near the Cape of Good Hope, (b) in the Gulf of Lion, (c) near the Cape Nao, and (d) western Greenland coast. The black line in right column shows average dependence of $W(u_{10})$ in 0.5 m bins.

dependence $W(u_{10})$.

Most of the data correspond to the wind velocity interval $u_{10}=7-11$ m/s with less data available for stronger winds ($u_{10}=12-15$ m/s) and few cases of extremely strong winds ($u_{10}>15$ m/s) (Fig. 5). The data are then fitted by the function $W = a * (u_{10} - U_0)^n$, where the fitting parameters defined by the least-squares method are $a = 8.9 \times 10^6$, $n = 2.5$, and $u_0 = 3$ m/s (shown by the red curve in Fig. 6), giving the following empirical relationship:

$$W = 8.9 \cdot 10^{-6} \cdot (u_{10} - 3)^{2.5} \quad (3)$$

The obtained parameterisation (the red line in Fig. 6) broadly fits the data (the black line in Fig. 6); however, under moderate wind conditions ($u_{10} = 8-12$ m/s), the whitecap coverage is slightly overestimated, and it is slightly underestimated during stronger winds (Fig. 5a).

A comparison of this parameterisation with those reviewed by Anguelova and Webster (2006) and (Brumer et al., 2017) is shown in Fig. 5b. This suggests broad consistency in the dependence $W(u_{10})$, indicating that the proposed method offers a reasonable quantification of whitecaps. However, the fitted curve plots in the lower region of the family of curves, suggesting an underestimation of whitecap coverage,

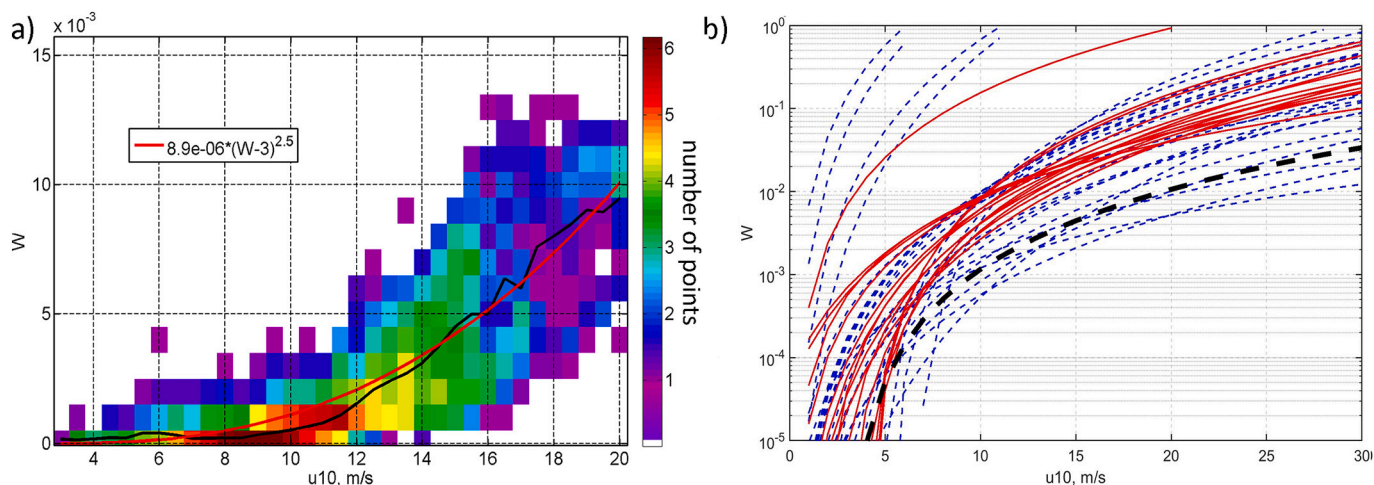


Fig. 5. a) Relation between whitecaps fraction W and the wind velocity u_{10} computed using quasi-synchronous Landsat-8 scenes and Ascats wind data. Colors show number of used measurements; Average empirical dependence of $W(u_{10})$ is shown by black curve, the red curve is fitted parameterization $W = 8.9 \times 10^{-6} * (u_{10} - 3)^{2.5}$. b) Comparison of the parameterization obtained in the present paper (black dashed line) with the others listed in (Anguelova and Webster, 2006 – blue line) and (Brumer et al., 2017 – red line) in logarithmical scale. (For interpretation of the references to colour in this figure legend, the reader is referred to the web version of this article.)

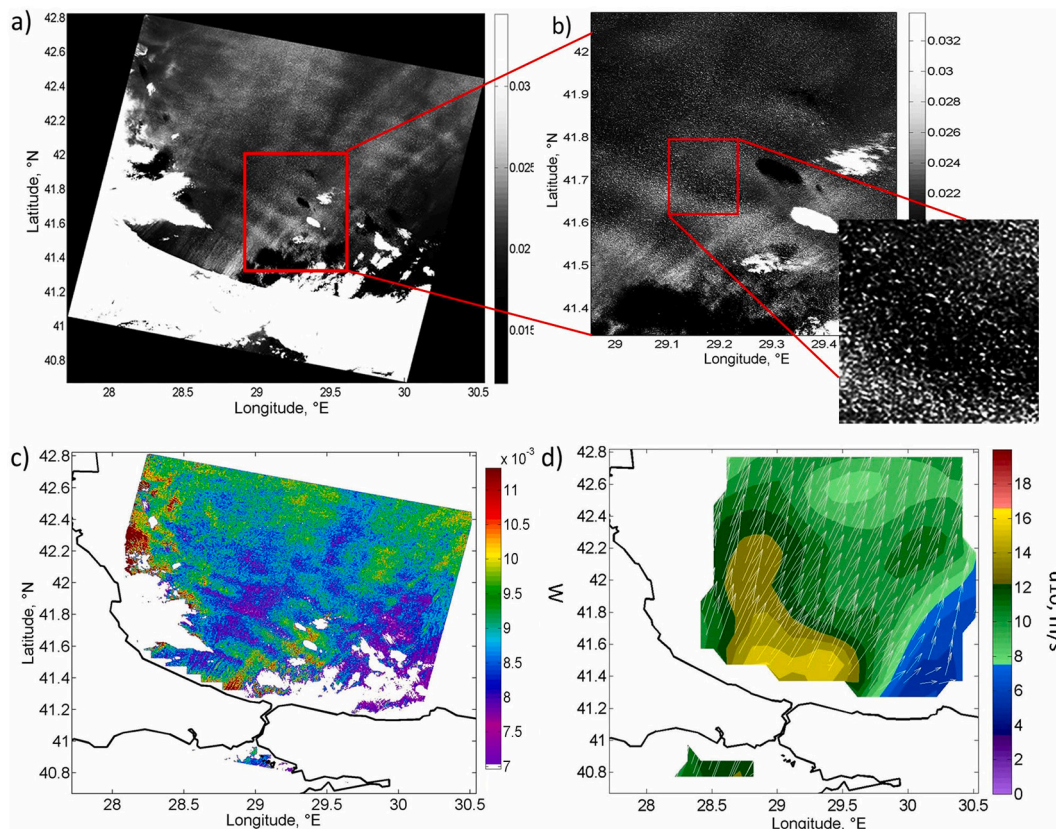


Fig. 6. a) Landsat reflectance centered at 865 nm near the Bosphorus strait for 12 January 2016. b) Zoomed fragment of the Landsat reflectance (shown by red rectangle in Fig. 6a) demonstrating impact of the atmospheric wave on the whitecap development. c) Calculated whitecap fraction d) Ascats wind velocity (m/s) for 12 January 2016; (For interpretation of the references to colour in this figure legend, the reader is referred to the web version of this article.)

especially in comparison with recent studies reviewed in (Brumer et al., 2017) (see the red lines in Fig. 5b).

Such underestimation is related to the relatively poor spatial resolution of the Landsat data, as the proposed algorithm identified only relatively large whitecaps above 3 m^2 (see Section 2.3). Small whitecaps that are more or less uniformly distributed at the sea surface will also

affect the background values of R_c but will not be detected as “large” whitecaps using the described method. The subtraction of R_c , which includes reflectance caused by small whitecaps, will further decrease the reflectance of whitecaps-affected pixels and the computed whitecap fraction using a fixed threshold.

Also, a noticeable scattering of data around the fitting line is

observed. For example, in Fig. 5a, at $u_{10} = 14$ m/s W, values range from 0.001 to 0.007 for the different Landsat scenes. There are several possible reasons for this scatter. First, the algorithm used is based on several assumptions that bring uncertainties to whitecap identification (see Section 2.3). Second, many other factors, such as atmospheric stratification, wave age, wave-current interaction, and bathymetry, can strongly impact (in addition to wind) wave breaking, as discussed in the following sections.

4.2. Wind speed variations: atmospheric waves

Bands of whitecaps oriented perpendicular to the wind direction can occasionally be seen in Landsat-8 images. In Fig. 6a and b, show Landsat reflectance at 865 nm near the Bosphorus Strait on 12 January 2016 when storm south winds with a velocity of 15 m/s were blowing over the Black Sea (Fig. 6d). Wind blowing from the mountainous areas of Turkey generated atmospheric internal waves, which induced oscillations in

near-surface wind speeds. These oscillations modulated the whitecap field with a wavelength of 20 km (Fig. 6c). Spatial variability in the number of bright spots (i.e. whitecaps) in the atmospheric waves is seen in the enlargement in Fig. 2b. The calculated whitecap coverage varies between 0.7% and 1.2% (Fig. 6c). According to Eq. (3), this corresponds to wind speed variations from 17 m/s to 20 m/s, i.e. wind speed modulation with an amplitude of 3 m/s in the atmospheric internal waves. Such wind-field features are not detectable by the scatterometer owing to their relatively low spatial resolution (Fig. 6d) but can be observed using a manifestation of whitecaps in high-resolution optical imagery. It should be noted that the variations in wind velocity change the mean surface slope, which affects the Fresnel bidirectional reflectance R_f . This effect also modulates the observed striped structure of R . However, whitecap reflectance is significantly higher than the Fresnel reflectance, which is related to the mean surface slope at moderate azimuth angles. The whitecap coverage is proportional to the cube of wind velocity, while the mean surface slope can be represented as a linear function

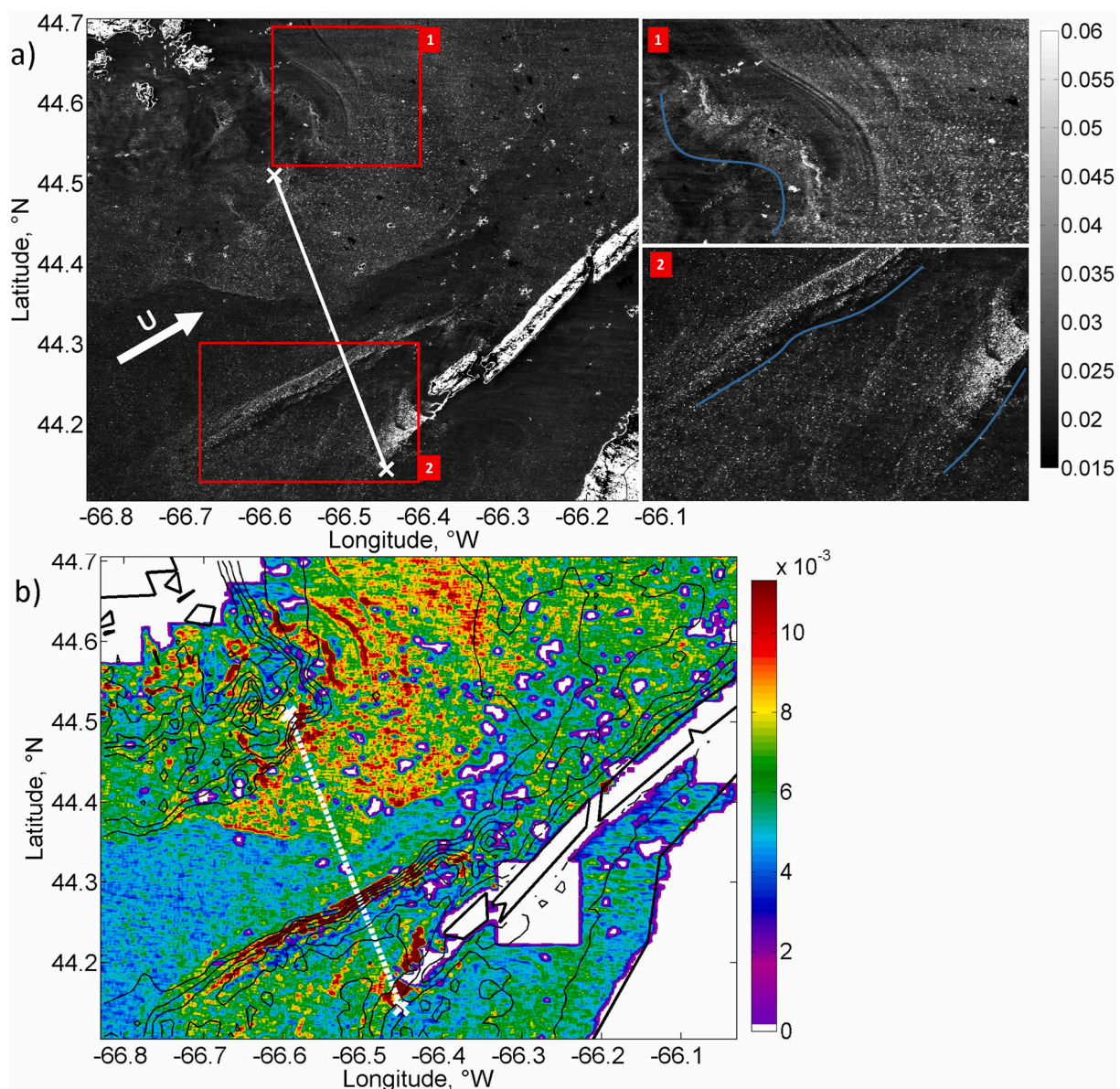


Fig. 7. a) Reflectance in channel 5 (865 nm) of Landsat-8 scene on 25 December 2014 over the Fundy Bay. Red rectangles #1 and #2 mark the areas used for the zoomed pictures shown on the right side of the figure. Blue lines highlight zones of maximal wave breaking; b) Whitecap fraction calculated from Landsat data. Black lines show the position of isobaths. White line indicates position of the section shown in Fig. 8e. (For interpretation of the references to colour in this figure legend, the reader is referred to the web version of this article.)

(Cox and Munk, 1954). Therefore, whitecaps should play a major role in the observed reflectance variations during such strong winds (17–20 m/s), which is clearly seen in the enlargement in Fig. 2b.

5. Manifestations of sub- and mesoscale ocean variability in whitecap fields

5.1. Bathymetry

Spectacular spatial variability in whitecaps caused by wave-current interactions in shallow water was observed in the Landsat-8 scene for 25 December 2014 in Fundy Bay near the eastern coast of Canada (Fig. 7). On this day, western storm winds with speeds of up to 15 m/s were blowing over the basin. Visual inspection of Fig. 7a reveals the high variability in whitecap distribution over the observed scene. This visual observation is confirmed by the calculated whitecap coverage map (Fig. 7b). In particular, in the northern part of the scene (indicated by red box #1 in Fig. 7a), several alternative bands of increased and dampened whitecaps are observed. These are possibly the result of the modulation of the whitecaps by trains of internal waves, which are discussed in more detail in Section 5.2. A curved band of increased whitecaps can also be seen in the western portion of this box. The position and form of this band show good agreement with the bathymetric slope in the area (shown by the black isolines in Fig. 7a).

The highest whitecap coverage values (Fig. 7b), which exceed 1%, were observed inside the areas marked by red rectangle #2 in Fig. 7. In enlargement Fig. 7a, it is seen that the increase in reflectance is caused by the strong increase in the number of randomly distributed bright spots (i.e. whitecaps). This spatial structure is different from the reflectance in convergence zone caused e.g. by the accumulation of

floating debris, which looks like a continuous line with increased reflectance. By comparing the whitecap map (Fig. 7b) with the bathymetry map (Fig. 8b), these enhanced whitecap areas are spatially linked to the bottom slopes of two oblong-shaped banks with depths of less than 30 m. This is also confirmed in the isobaths overlay in Fig. 7b.

Transects of whitecap coverage, bathymetry, and wind speed across the bay (shown as white lines in Fig. 7a and b) demonstrate these features in more detail (Fig. 8c). Three sharp peaks (P1, P2, and P3) in W (black line) exceeding 1% are situated at latitudes 44.18°N, 44.27°N, and 44.5°N, respectively. Peaks P2 and P3 are located at the peripheries of the deep part of the bay in zones with sharp bottom slopes where the depth changes from 200 m to 50 m (see the red line in Fig. 8c). Their positions closely correspond to the zone of isobath convergence in Fig. 7b and coincide with the same peaks in bathymetry gradients (see the magenta line in Fig. 8c). The southern peak (P1) is located on the periphery of a shallow bank (depth = 30 m) that extends from Long Island and Brier Island. This maximum W is located not in the shallowest area of the bank but over the bank slope with high bathymetry gradients in its northern part.

The correlation between enhanced whitecap coverage and depth gradients has a clear physical explanation. First, we found that whitecaps visualise the process of wave-breaking dissipation in wind-waves, and a fraction of the whitecap coverage is proportional to the wind energy input (Phillips, 1985). Wave-current interaction acts as an energy input or energy sink to waves, which should be compensated by the increase or decrease in wave-breaking dissipation, respectively. In the latter case, clear signatures of currents form on the sea surface.

As argued by Kudryavtsev et al. (2005), among different components of the surface current velocity shear, the main impact of currents on variations in wind-wave parameters integrated over the azimuth, such

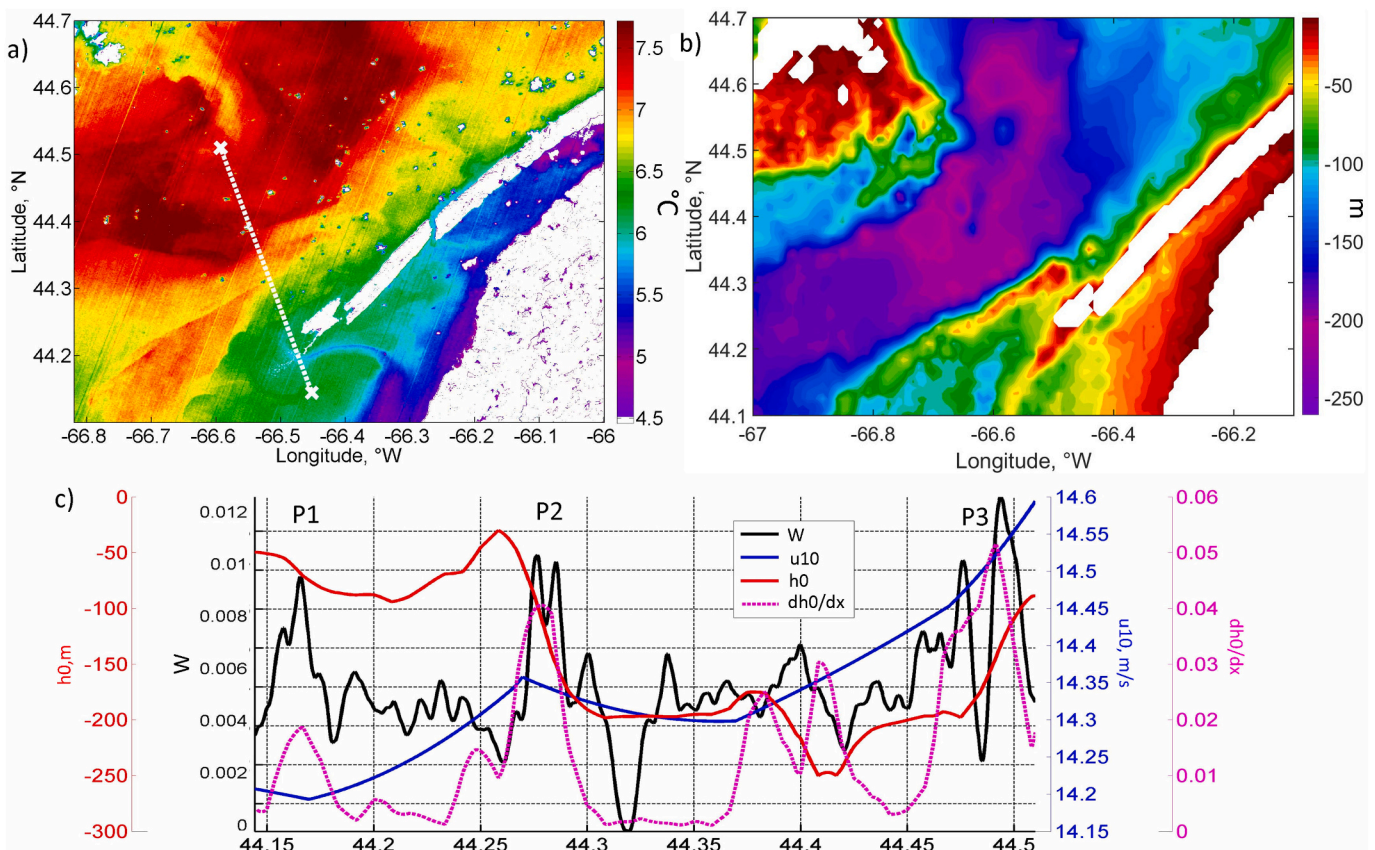


Fig. 8. a) SST (°C) from Landsat-8 channel 11 in the Fundy Bay at 26 December 2014; b) Gebco bathymetry (m); c) Transect of the whitecap coverage (black line), Gebco bathymetry (red line), bathymetry gradients (magenta line), and Ascet wind (blue line). The position of the section is shown by the white dashed line in Fig. 7, 8a. (For interpretation of the references to colour in this figure legend, the reader is referred to the web version of this article.)

as whitecap coverage, is due to current divergence. In this case, whitecap coverage in the presence of non-uniform currents is described as follows:

$$W = W_0(u_*) \left(1 - b \frac{g^{1/2}}{u_*^2 k_b^{3/2}} \nabla \cdot \mathbf{u} \right) \quad (4)$$

where u_* is the air friction velocity, $W_0(u_*)$ is the background (i.e. no current) value of the whitecap coverage, k_b is the wavenumber of the shortest breaking waves forming whitecaps, b is a constant, $u_* = \sqrt{Cd} * u_{10}$ with $Cd = 1.5e-3$, and $\nabla \cdot \mathbf{u}$ is the surface current divergence. According to observations (e.g. Korinenko et al., 2018), the phase velocity of the shortest gravity waves generating observable whitecaps is approximately 2.5 m/s. Using the dispersion relation, k_b in Eq. (4) should be $k_b = 1.6$ rad/m. This cut-off wavenumber is in accordance with the minimum size of breakers detectable in Landsat imagery (see Section 2.2). Following Kudryavtsev et al. (2012, see Eq. 17), the constant b in Eq. (4) can be assigned as 400. Using these numbers, we estimate that the surface current convergence of a current with the

magnitude $\nabla(\mathbf{u}) = 0.5 * 10^{-3}$ 1/s at a wind speed of 10 m/s should lead to whitecap enhancement by a factor of 3. Current divergence with the same magnitude should lead to the disappearance of the whitecaps. These estimates are similar to those reported by Dulov and Kudryavtsev (1990).

Thus, the divergence of a surface current with an arbitrary origin should impact spatial variations in whitecap coverage, leading to the enhancement of a convergent zone (where $\nabla \cdot \mathbf{u} < 0$) and suppression in divergence (where $\nabla \cdot \mathbf{u} > 0$). In shallow water, divergence of surface currents can be caused by the interaction between the main flow and bottom topography. Continuity of the water masses integrated over the depth suggests that interaction between the current velocity field, \mathbf{u} , and bottom slope, ∇h , produces surface current divergence, thus:

$$\nabla \cdot \mathbf{u} = h^{-1} \mathbf{u} \cdot \nabla h \quad (5)$$

Eqs. (5) and (4) explain the visual correlation between the bottom slope and whitecap coverage anomalies in Fig. 7b and Fig. 8c.

Similar features were also detected in Synthetic-Aperture Radars data (SAR) in (De Loor, 1981; Yu et al., 2016). The divergence of depth-

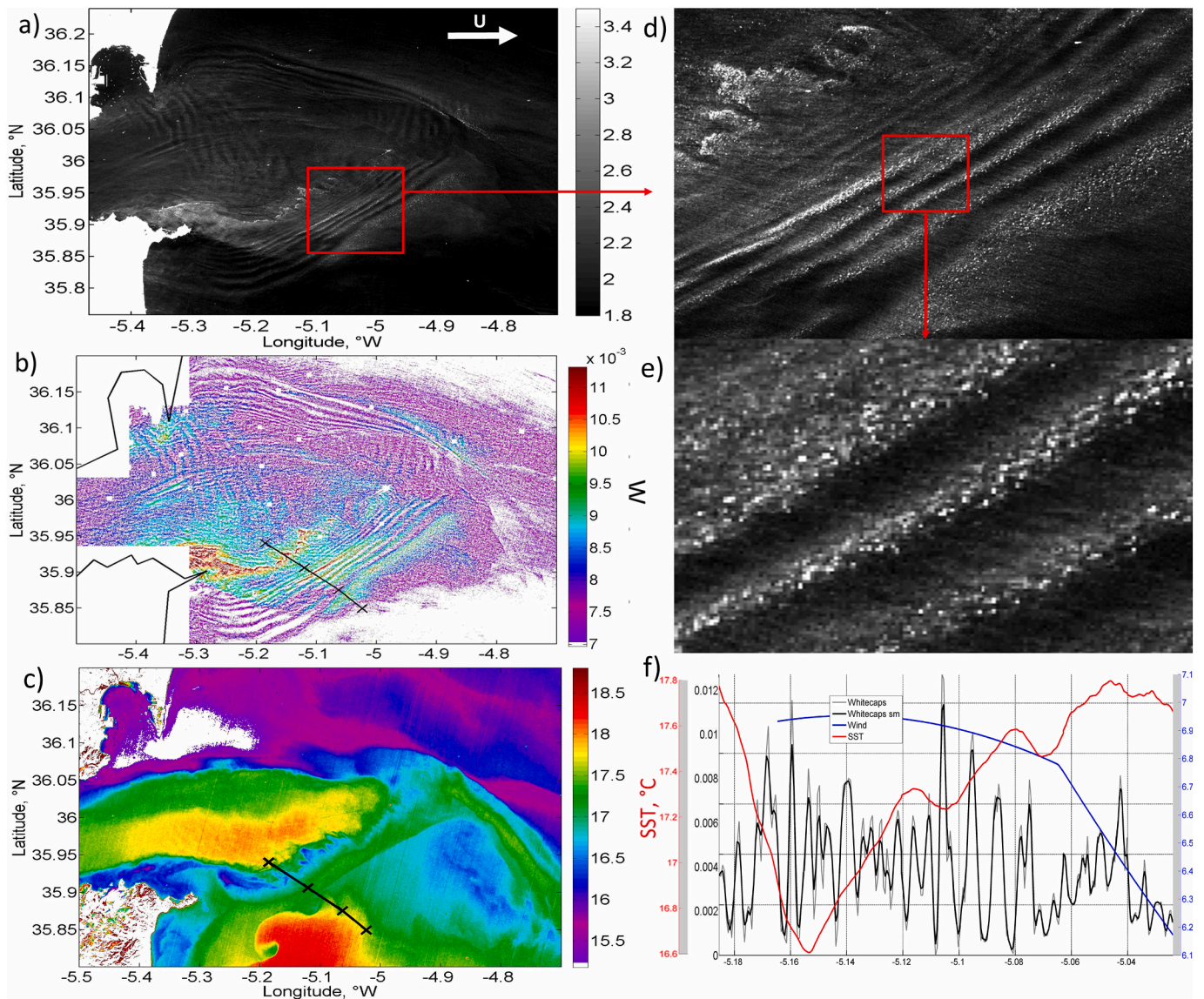


Fig. 9. The effect of internal wave on the wave breaking: a) Landsat 8 measurements of the reflectance in channel 5 for 11 June 2013; White arrow shows the dominant direction of the wind. Fig. 9d and Fig.9e showed zoomed part of the scene. b) Whitecap fraction calculated from the reflectance data; c) SST brightness temperature in the Landsat 10 channel; f) Transect of the whitecap fraction (black line), SST (red line), and Ascet wind (blue line). The position of the Section is shown in Fig. 9a-c. (For interpretation of the references to colour in this figure legend, the reader is referred to the web version of this article.)

gradient-induced currents results in wave-breaking anomalies, which impact the radar scattering and lead to a bottom topography signature in the SAR images.

5.2. Internal waves

Convergence/divergence of the surface currents induced by internal waves (IW) on the ocean surface leads to strong modulations in whitecap coverage (e.g. Dulov et al., 1986; Thorpe et al., 1987; Dulov and Kudryavtsev, 1990). This effect is well seen in the vicinity of the Gibraltar Strait in the Landsat scene for 11 June 2013 (Fig. 9a). Intense IWs in this area are primarily generated by the interaction of tidal flows with prominent underwater bottom features (Boyce, 1975; Brandt et al., 1996).

In the Landsat images at a reflectance of 865 nm (Fig. 9a), trains of IWs manifest as alternating bright/dark bands associated with the enhancement/suppression of wave breaking. The increase in the number of bright-spot whitecaps in the zone of convergence and their almost complete absence in the zone of divergence caused by internal waves is seen in the enlargements Fig. 9b and e. Whitecap coverage derived from this image exhibits strong modulation in wave-breaking intensity, with a peak-over-trough ratio in the order 10 (Fig. 9b). The wind speed at the moment of the Landsat survey was approximately 7 m/s, with an eastward direction. According to Eq. (3), the whitecap coverage for such a wind speed should be small, approximately 0.1%. However, the modulation of whitecaps by the IWs led to a significant deviation in W from this background value. Referring to Fig. 9b, W in the convergence zones is approximately 1% and effective zero in the divergence zones (Fig. 9e).

Fig. 9f demonstrates a transect of whitecaps, wind, and SST fields along the line shown in Fig. 9b and c. Despite the almost uniform wind speed distribution, the whitecap coverage oscillates in the range 0.02–1%. W peaks (1.2%) at longitudes of 5.16°E and 5.105°E. This area corresponds to a local decrease in surface temperature (shown by the red line). The formation of this cold area is likely due to intense upwelling or mixing at the periphery of the Atlantic Jet (Sarhan et al., 2000). The maximal values of W are slightly displaced to the west, from the minimum SST, and are located in the zones of high SST gradients, i.e. in the vicinity of the frontal zones where horizontal current shear is probably high and dynamics modulate the wave breaking (see Eq. 4).

Field observations of wave-breaking modulation by IWs were reported by Dulov et al. (1986). These authors report that the divergence of IW-induced surface currents led to strong modulations in wave breaking with transfer functions (the ratio of wave breaking contrasts to the thermocline displacement amplitude over depth) in the order of 10, which is similar to our observations. In this context, the divergence of IW-induced currents and thermocline displacement using observed modulations of whitecaps and Eq. (4) can be assessed. Based on Eq. (4), divergence in IW-induced currents on the surface can be expressed based on the observed white caps modulations as follows:

$$\nabla \cdot \mathbf{u} = \left(\frac{W}{W_0} - 1 \right) \frac{u_b^2 k_b^{3/2}}{bg^{1/2}} \quad (6)$$

When $k_b = 1.6 \text{ rad/m}$, $b = 400$, wind speed $u_{10} = 7 \text{ m/s}$, the whitecap background value $(W_0) = 0.3\%$, and the mean peak value $(W) = 1\%$, we obtain the following estimate of divergence: $\nabla \cdot \mathbf{u} = 6 \cdot 10^{-4} \text{ 1/s}$. For the pycnocline displacement described by harmonic oscillations, $h(x, t) = h_0 + a \cos(\mathbf{K} \cdot \mathbf{x} - \Omega t)$, the amplitude of the surface IW-induced current divergence is as follows:

$$\nabla \cdot \mathbf{u} = \left(\frac{a}{h_0} \right) \Omega = \left(\frac{a}{h_0} \right) KC \quad (7)$$

where a and h_0 are the amplitude and undisturbed value of pycnocline depth; K , Ω , and C are the IW wavenumber, frequency, and phase velocity linked by the dispersion relation $C = \sqrt{(\Delta\rho/\rho)gh_0}$; $\Delta\rho/\rho$ is the density drop over the pycnocline scaled by the mean density value.

Based on Fig. 9, IW wavelength varies from 400 m to 1 km. Evaluating $\Delta\rho/\rho$ and h_0 from climatic data (Ovchinnikov and Plakhin, 1976; Brasseur et al., 1996), where $\Delta\rho/\rho = 0.003$ and $h_0 = 150 \text{ m}$, then $C = 2 \text{ m/s}$, giving an estimate of $a = 9\text{--}18 \text{ m}$, which is in broad agreement with previous studies on internal waves in the study area (e.g. Vlasenko et al., 2009). This suggests that measured modulations in whitecaps can provide useful information about the dynamic properties of IWs.

5.3. River plumes

Fig. 10 shows the whitecap distribution during the development of an intense northwest katabatic wind jet (Mistral) in the Mediterranean Sea with wind velocities of more than 20 m/s on 25 January 2015.

The prominent feature in Fig. 10 is the effect of the Rhone River plume on wave breaking. Inside the plume, the whitecap fraction decreases noticeably compared to the surrounding waters. W in the plume is approximately 0.1% or less, which is lower than in the surrounding area by a factor of four ($W = 0.5\%$) (Fig. 10a and c). One of the most plausible reasons for this is the effect of atmospheric stratification, which is more stable over cold plume water. The temperature at the Rhone River mouth is 7 °C, which is lower than the surrounding waters with a SST of approximately 10 °C (Fig. 10b). The cold river waters alter the atmospheric stratification, leading to the suppression of turbulence and surface wind stresses, and consequently, wind-wave forcing and dissipation via wave breaking. This phenomenon has been observed and reported in several studies. In particular, field experiments by Kudryavtsev et al. (1996) revealed changes in the vertical shear of wind velocity and air temperature, which correlated well with spatial differences in SST. Coincident shipborne radar measurements revealed stronger radar scattering from locally warm surface areas and weaker scattering from locally colder surface areas. Beal et al. (1997) reported a similar depression in radar returns on the cold side of the Gulf Stream front and enhancement on its warm side.

To provide quantitative estimates of the impact of stratification on whitecap distribution, we first observed that variations in the whitecap coverage, \tilde{W} , are caused by changes in friction velocity, \tilde{u}_* . The empirical relation in Eq. (3) suggests that W depends on u_* as $W \propto u_*^{-3}$ (following Phillips, 1985), and thus $\tilde{W}/W = 3\tilde{u}_*/u_*$. If we assume that the parameters of the free atmosphere (geostrophic wind speed and temperature) are horizontally uniform at the scale of SST fronts, then any variations in surface stress result from planetary marine atmospheric boundary layer transformation over the spatially variable SSTs. The response of friction velocity to SST variations, \tilde{T}_w , is described by Kudryavtsev et al. (2005, see Eq. (59) and Fig. 9) as $\tilde{u}_*/u_* = [1/(2C_D)\partial C_D/\partial T_w] \tilde{T}_w$. Assuming that atmospheric stratification outside the plume is neutral, we estimated the transfer function $1/2\partial(\ln C_D)/\partial T_w$ for the considered wind conditions as $1/2\partial(\ln C_D)/\partial T_w \approx 0.08$ (Kudryavtsev et al., 2005). Thus, the relationship between variations in whitecap coverage and W_0 outside the plume (where SST = 11 °C) can be written as:

$$\frac{W}{W_0} = 1 + 0.24(T_w - 11) \quad (8)$$

Although this is a linear estimate, it is in quantitative agreement with W as shown in Fig. 10, predicting a decrease in $W_0 = 3.5\%$ outside the plume to $W = 0.5\text{--}1\%$ in the plume where $T_w = 7.5\text{--}8 \text{ °C}$.

An additional factor that can lead to a decrease in W in the plume is the increase in water viscosity due to the presence of surfactants, and decreases in water temperature. These effects increase the surface tension and dampen the generation of bubbles during wave breaking (Monahan and O'Muircheartaigh, 1986; Callaghan et al., 2014; Hansen et al., 2016).

Another prominent feature in Fig. 10a and c is a linear zone of enhanced reflectance at the southern boundary of the river plume oriented perpendicular to the wind direction. Wind moves the plume to the

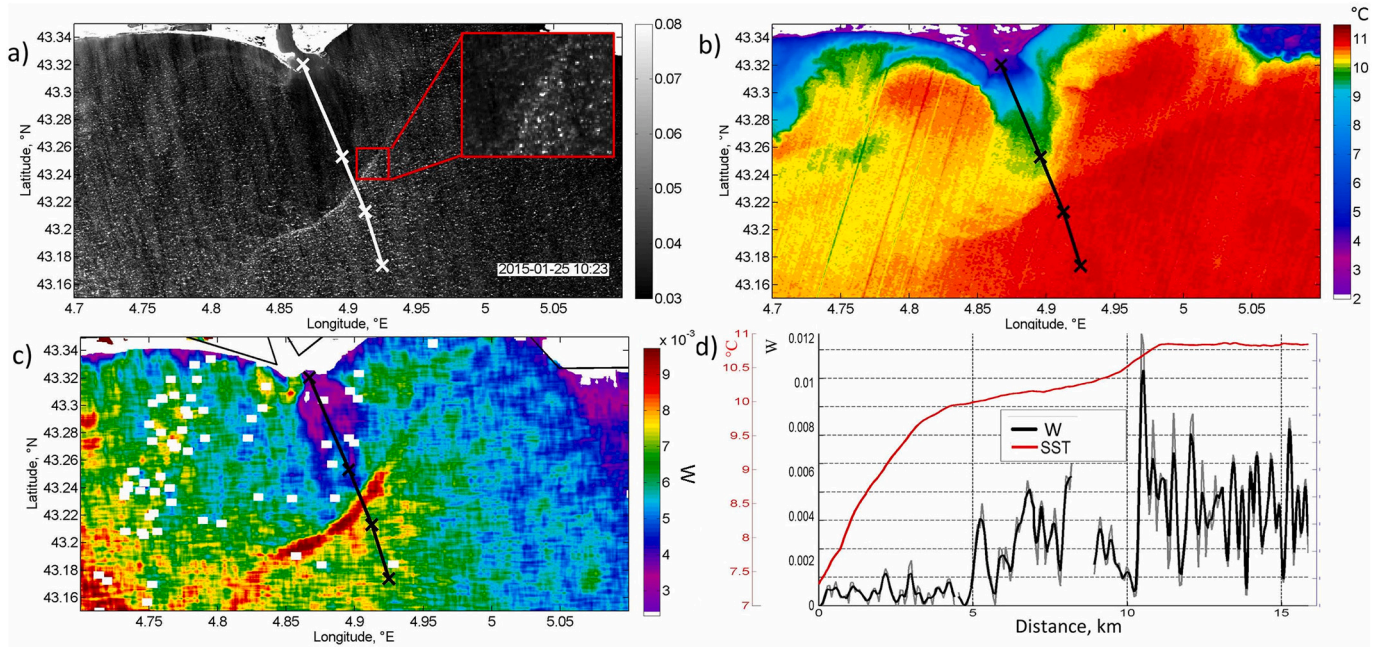


Fig. 10. The effect of river plume on whitcaps field: a) Landsat-8 reflectance at channel 5 0.845–885 nm over the Rhone mouth, Mediterranean Sea, during the development of the Mistral winds on 25 January 2015. Red rectangle shows zoomed part of the scene. b) SST from Landsat 10 channel; c) Calculated whitcap fraction; d) Section of the whitcaps fraction (black line – whitcap fraction smoothed with 10-point filter) and SST (red line). X-axis is in km. The position of the section is shown in Fig. 10a-c. (For interpretation of the references to colour in this figure legend, the reader is referred to the web version of this article.)

south, where riverine brackish waters collide with salty seawater. A strong salinity front causes convergence, which intensifies the wave breaking in this area. It should be noted that another possible reason for the rise in reflectance is the accumulation of floating material, e.g. blooms of cyanobacteria at the plume front. In this case, cyanobacteria or floating debris are distributed in thin extended lines along the front (Aleskerova et al., 2019; Qi et al., 2020). However, in the given example, the rise in reflectance during the strong winds was caused by an increase in the number of bright whitcaps (see the enlargement in the upper right-hand corner of Fig. 10a). This wave-breaking enhancement traces the linear zone of convergence separating the inflowing river water, accelerating via the action of wind from the surrounding water. A similar effect was detected and studied experimentally by Thomson et al. (2014) and Zippel et al. (2018). The strong impact of surface current convergence on wave-breaking intensity has also been previously suggested and experimentally demonstrated (Dulov and Kudryavtsev, 1990; Kudryavtsev et al., 2005, 2012, 2014; also see Section 5.4).

In Fig. 10d, the transect of the whitcap fraction and SST across the plume (shown as a black line) demonstrates that W was very small in the low-temperature area ($SST = 2\text{--}10\text{ }^{\circ}\text{C}$) and increased to 0.3% where SST reached $10\text{ }^{\circ}\text{C}$. Whitcap coverage sharply increased up to 1% in the vicinity of the plume boundary (convergence zone) and, outside the plume (on the seaward side), maintained a constant value of 0.5%. Such strong wave breaking around the plume boundary may significantly strengthen the mixing of river and sea waters, weakening horizontal salinity and temperature gradients (Thomson et al., 2014; Zippel et al., 2018).

5.4. Convergence/divergence zones and SST frontal features

Enhancement of wave breaking in the vicinity of ocean fronts is routinely observed in Landsat scenes. One example is shown in Fig. 11, where two linear zones of enhanced W in the Gulf Stream area were observed on 20 November 2014 (Fig. 11a and b). The linear zone adjoining the northern edge of the Gulf Stream is the most prominent feature of the whitcap field (Fig. 11b and Fig. 11c). The other linear zone adjoins the temperature gradient in an area of cold shelf waters. In

the front area, the whitcap fraction is twice as high (1.1%) as in the surrounding waters (0.6%).

Wind fields, in this case, were almost uniform and directed to the northeast ($u_{10} = 10\text{--}11\text{ m/s}$). It is worth noting that the whitcap coverage in the cold Labrador water area is larger (mean $W = 1\%$) than in the area of warm SSTs (mean $W < 0.5\%$). Such whitcap behaviour conflicts with the anticipated trend discussed in Section 5.3, as the effect of atmospheric stratification should lead to larger W over warm waters. This “aberration” is probably caused by other factors and mechanisms including non-linear Ekman pumping, which can suppress wave breaking. Notably, this effect has also been observed in association with the Gulf Stream (Liu et al., 2016).

Based on Eq. (4), the convergence/divergence of surface currents is one of the governing parameters causing enhancement/suppression of wave-breaking intensity. The divergence field can be estimated from Landsat thermal data using the approach suggested by Kudryavtsev et al. (2012). Following this approach, convergence/divergence of surface ocean currents can result from the interaction of wind-driven currents with the vorticity of surface quasi-geostrophic (SQG) currents. Reconstructing SQG from a snapshot SST image (Isern-Fontanet et al., 2006) and using a classical solution for the Ekman current (slab-model), the following relationship for surface divergence (in Fourier space) was obtained (see Kudryavtsev et al., 2012, and Section 3.1 for more details):

$$\widehat{\nabla} u = \frac{i\alpha}{\gamma^{1/4} n_b^{1/2}} \cdot \frac{g v_*}{f^2} \sin(\varphi_w - \varphi) K^2 \widehat{T}_s \quad (9)$$

where a hat operator denotes Fourier transform; $n_b = N/f$ is the Prandtl ratio for the Brunt-Väisälä frequency, N , determining mesoscale properties of the flow; f is the Coriolis parameter; g is gravity acceleration; α is the thermal expansion coefficient; $\gamma = 0.2$, v_* is the friction velocity in the water; φ_w is the wind speed direction; and K and φ are the modulus and direction of the wavenumber vector, respectively. Eq. (9) describes the relationship between current divergence and SST in Fourier space. The inverse Fourier transform of Eq. (9) provides current divergence in physical space. Consequently, as $K^2 \widehat{T}_s$ corresponds to the Fourier transform of the SST Laplacian, convergence/divergence of mesoscale

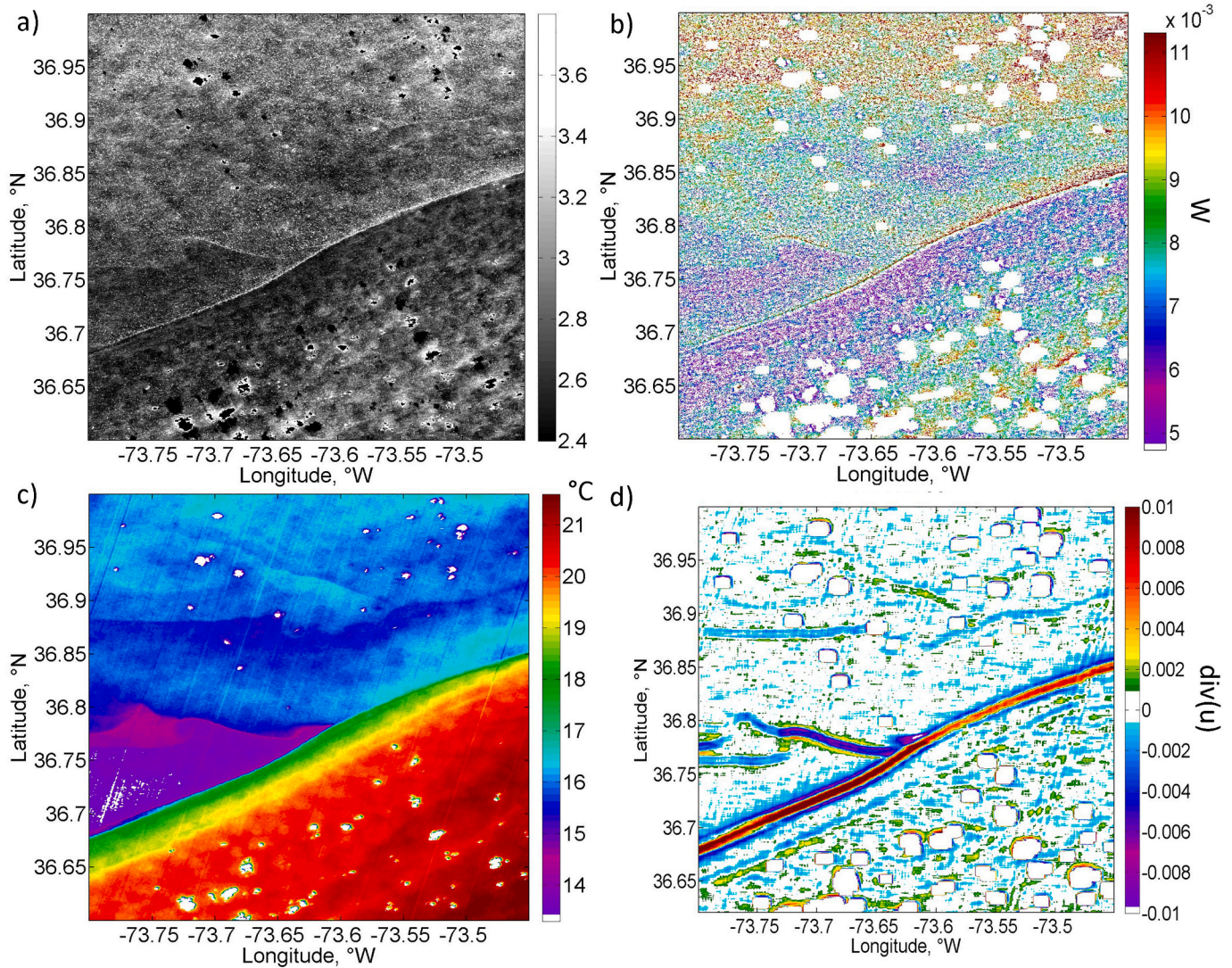


Fig. 11. The manifestation of the small-scale ocean fronts in the vicinity of the Gulf Stream on 20 November 2015: a) Landsat brightness in channel 5; b) whitecaps fraction calculated from Landsat data; c) SST from Landsat-8 channel 11; d) current divergence derived from Landsat-8 thermal channel 11 following (Kudryavtsev et al., 2012; their Eq. (16)).

ocean current broadly trace the Laplacian of the SSTs, the full equation for which is given by Kudryavtsev et al. (2012). This qualitative estimate is confirmed by the location of the model convergence/divergence zones, which are linked to the maximum SST gradients (compare Fig. 11d and c).

The calculated divergence (Fig. 11d) corresponds well to the enhanced whitecap anomalies depicted in Fig. 11b. The divergence along the northern edge of Gulf Stream is quite high, with values varying from 0.006 to 0.01 1/s, and is related to the very sharp temperature front, which changes by 6 °C in a 200-m-wide frontal zone. Thus, the sharp increase in the wave breaking illustrates the significance of vertical motion in the vicinity of the fronts and their strong potential for the weakening and destruction of the front, and mixing of physical and biochemical properties, in the frontal zone. Note that Eq. (9) describing the divergence of secondary circulation, which results from the interaction of Ekman flow with SQG currents, is essentially based on the assumption that the Rossby number is small. However, considering local ocean current features with a sharp velocity gradient (as in Fig. 11 and Fig. 12, described below), one may anticipate that this assumption no longer holds. In this context, Eq. (6) must be used to derive qualitative estimates, particularly as a physical basis for the interpretation of the link between wave-breaking anomalies and SST features. Quantitative

aspects of this link require more elaborate model development.

Another notable example of a similar effect was observed in the Azov Sea on 13 November 2015 when intense northeast winds (> 10 m/s) were blowing. These winds probably caused upwelling on the eastern periphery of the Azov Sea, which cools its northeast part. From the east coast of the Azov Sea, upwelling waters elongate to the east and form a filament with a well-defined cold mushroom structure (M1) at its end (Fig. 12c). The length of the filament was approximately 50 km and its width was approximately 40 km.

This structure was clearly manifested in the whitecap field near IR reflectance in Fig. 12a and b. The position of the whitecaps strictly corresponds to the “stipe” of M1 (Fig. 12b). We can also observe the north-south asymmetry of the whitecap distribution. In the northern part of the stipe of M1, the whitecap coverage decreases whereas it increases in the southern part. At the same time, as in the previous case, wave breaking was almost absent in the relatively warm waters to the north and south of the structure. Very complex dynamic processes seem to take place at the mushroom “cap” (see boxes #1 and #2 at the top of Fig. 12). A zone of increased whitecaps surrounds the “cap” at its edge, while at its centre, relatively calm waters are observed with no whitecaps. This can also be explained by divergence/convergence patterns in this complex dynamic structure. Fig. 12d demonstrates the divergence

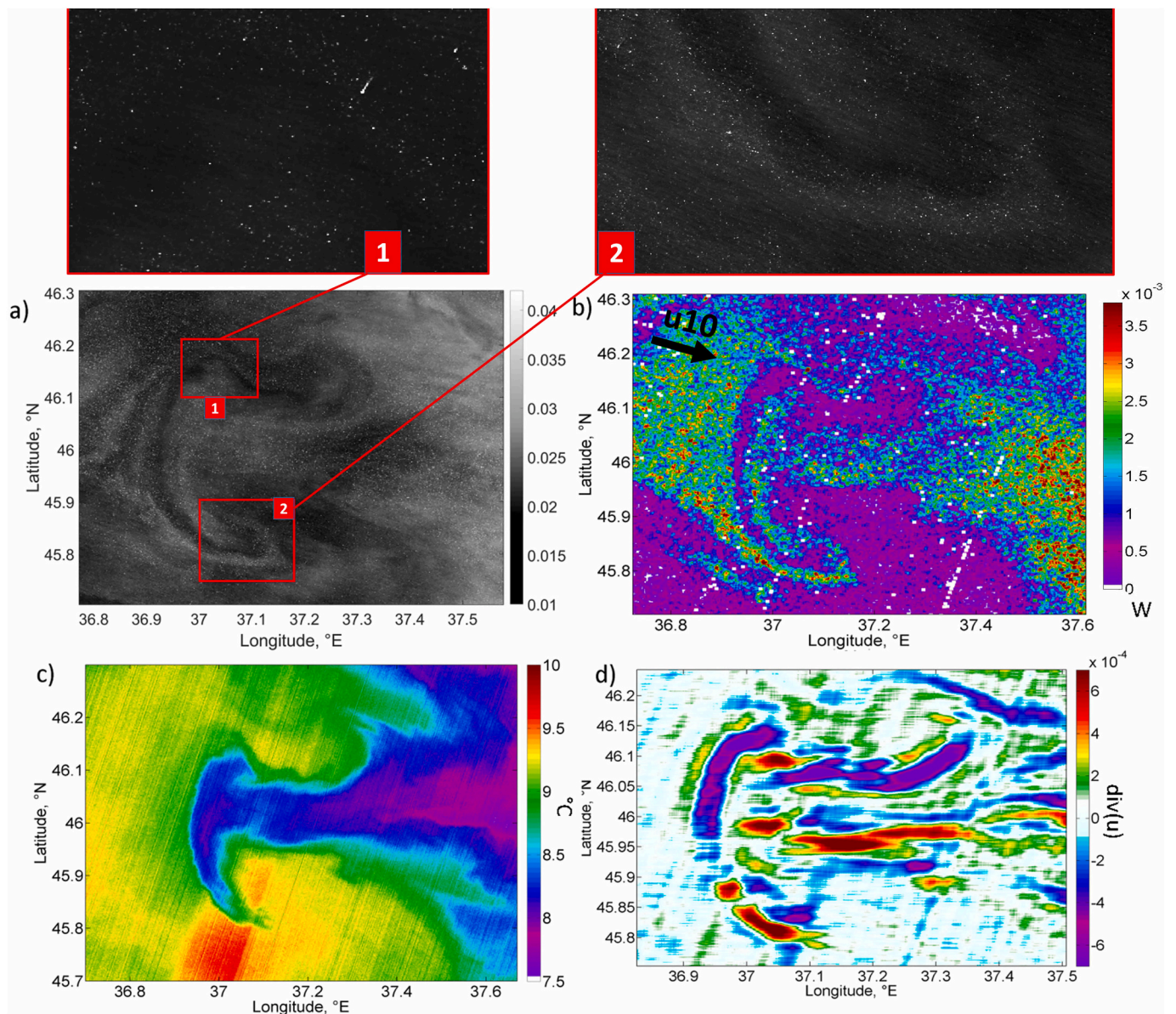


Fig. 12. Impact of mushroom current on whitecaps distribution: a) Landsat brightness in channel 5 in the Azov Sea on 13 November 2015; Red rectangles #1 and #2 mark the areas used for the zoomed pictures shown on the top side of the figure. b) Whitecap fraction calculated from Landsat data; Black arrow show the direction of the wind. c) SST from Landsat-8 channel 11; d) Divergence of currents calculated from Landsat-8 thermal channel 11 using (Kudryavtsev et al., 2012). (For interpretation of the references to colour in this figure legend, the reader is referred to the web version of this article.)

field computed from Landsat thermal data using the SQG computation method described above (Kudryavtsev et al., 2012). The position of the divergence zone (blue colour) is in agreement with low W values at the north side of the mushroom current and in the centre of its “cap”. The position of the convergence zone coincides with intense wave breaking at its south part and around the “cap”.

Usually, mushroom currents are formed as a result of the rapid slowing down of offshore currents (Fedorov and Ginsburg, 1989). This should be accompanied by the emergence of zones of intense convergence where the filament collides with surrounding waters, as observed on the outer periphery of the computed field. Due to current deceleration, in the centre of the “cap”, the water began to diverge, flowing north and south to form two eddy structures on each side of M1. The strain of the flow induced by the forming dipole eddy is the probable reason for the observed divergence and decrease in W in the centre of the “cap”.

North-west asymmetry in the convergence-divergence pattern is probably caused by the interaction of the current in M1 with the wind

field. The currents in the northern part of the “cap” are directed downwind; therefore, the total wind stress is reduced (see Section 5.5) and divergence is observed in the northern part of the M1 “cap”. At the same time, in the stipe, current and wind are opposite, and wave breaking intensifies.

5.5. Impact of “large-scale” surface motion on the wind stress

Wind stress depends on the wind velocity relative to the moving surface. If the direction of the winds and intense currents are opposite, wind stress will increase; otherwise, it will decrease. This can be accounted for by the modified resistance law, thus:

$$u_*^2 = C_D(\mu)|\mathbf{G}-\mathbf{U}|^2 \tag{18}$$

where G is the geostrophic wind velocity and U is the velocity of the surface currents. This effect can be significant in whitecap formation as

$W \sim u^3$ especially for low-to-moderate winds.

This effect can partly explain the decrease in whitecaps over the warm Gulf Stream waters discussed in Section 5.4. The larger part of the Landsat-measured scene, SST, and calculated whitecap field for the scene on 20 November 2014 over the Gulf Stream are shown in Fig. 13a and b. The whitecap coverage was generally lowest ($W < 0.3\%$) over cold Labrador waters (SSTs $< 16^\circ\text{C}$). Another W minimum is observed in the warmest waters, denoted by the area with SSTs $> 22^\circ\text{C}$. Over the Gulf Stream (with SSTs approximately $20\text{--}22^\circ$), the whitecap fraction (W) significantly decreases 0.1–0.4% and later increases at a distance of 40 km from the front (Fig. 13a and b). This area with the warmest waters corresponds to the centre of the Gulf Stream jet (Fig. 13c), as confirmed by the satellite altimetry data. A map of geostrophic velocities in Fig. 13d shows that the Gulf Stream is directed to the northeast and has a velocity of 1–1.6 m/s.

The velocity of geostrophic winds calculated from the Merra reanalysis changes from 11 m/s in the southern part of the scene to 14 m/s in the northern part (Fig. 13d). Geostrophic winds show no visible features related to the Gulf Stream impact, although they are directed in the Gulf Stream course. Therefore, the velocity of airflow relative to the surface over the Gulf Stream (see Fig. 13e) will be less on the current velocity. According to Eq. (18), the wind stress will be $G^2/(G-U)^2 = 12.5/(12.5-1.5)^2 = 1.3$ times lower. As whitecap coverage is proportional to u^2 W will be lower by a factor of 2. Fig. 13f shows W computed from wind velocity using Eq. (3), as described in Section 4.11. This map demonstrates a two-fold decrease in whitecap coverage in the Gulf Stream, especially in its southern part. This is in agreement with the Landsat data in Fig. 13b and confirms the important role of “large-scale” surface motion on wave breaking in the areas of strong currents.

The highest W values (0.8–1.2%) were observed on both sides of the Gulf Stream, especially in a strong, relatively warm cyclonic meander with SSTs of $18\text{--}20^\circ$, which detaches from the western border of the Gulf Stream. This meander is clearly visible in the SST map in Fig. 13c but absent in the relatively low-resolution altimetry data. The geometry of

the meander suggests that its currents are directed to the south, against the wind, which will increase wave breaking. This is indeed observed in the Landsat data (Fig. 13b); however, the meander is absent in the altimetry data and, as such, cannot be adequately described using wind reanalysis and satellite altimetry in Fig. 13f.

6. Conclusions

Landsat-8 measurements with a high signal-to-noise ratio provide a good opportunity to observe wave breaking from space over the global ocean. One Landsat scene covers an area of approximately $200\text{ km} \times 200\text{ km}$, which cannot be properly captured even by airborne photography. Freely available high-resolution Landsat-8 and Sentinel-2 data provide the possibility to study the variability of whitecaps over a wide range of scales, from hundreds of metres to meso- and global-scales, and to investigate the dependence of this variability on environmental atmospheric parameters (e.g. wind speed and stratification) and ocean processes (e.g. currents of different origin and ocean fronts). A method of retrieving the fraction of the ocean surface covered by whitecaps from reflectance measurements in the NIR channel with $30 \times 30\text{ m}^2$ spatial resolution has been proposed in this study. A combination of satellite scatterometer data and Landsat-8 optical imagery provides unique information on quasi-synchronous wind and whitecap distribution in the open ocean. We obtained more than 40,000 quasi-synchronous wind-whitecap estimates averaged into $1/8^\circ$ bins to estimate the dependence of the whitecap fraction on wind speed. Such a large amount of data may lead to significant improvements in our knowledge of wave breaking and wave dissipation in the open ocean under different wind conditions.

Due to its specific measurement capabilities, Landsat data provide a unique opportunity to investigate the impact of sub- and mesoscale ocean dynamics, and ocean SST fronts, on wave breaking fields. We have suggested a framework for investigating the impacts of various ocean phenomena and processes on whitecap variations including shallow

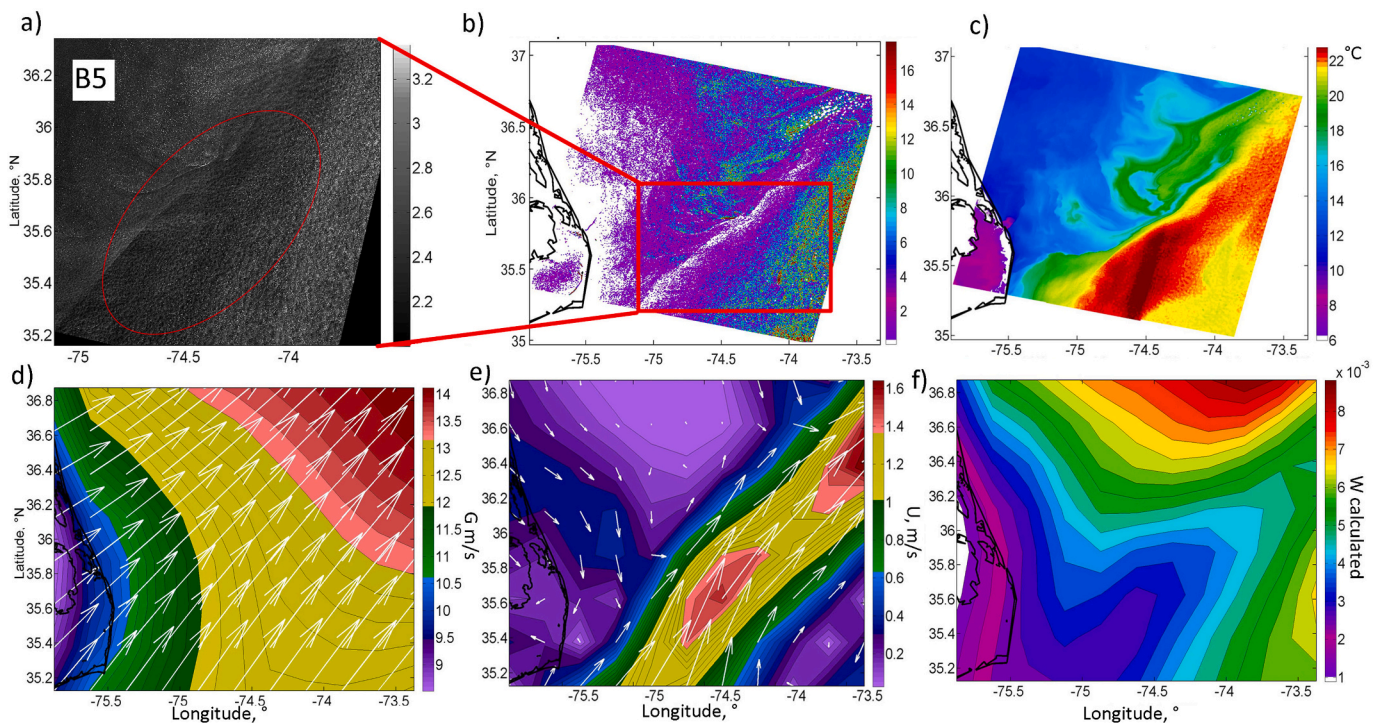


Fig. 13. Effect of the surface motion on whitecap distribution: a) Landsat brightness in channel 5 in the vicinity of the Gulf Stream on 20 November 2015. Whitecaps are dampened in the warm Gulf stream jet. b) Whitecap fraction calculated from Landsat data c) SST from Landsat-8 channel 11; d) Geostrophic wind velocity relative to the surface currents from Merra reanalysis (G); e) Altimetry-derived geostrophic currents at 20 November 2015; f) Whitecap fraction (W) calculated from wind and altimetry data using eq.1.

water bathymetry, internal oceanic and atmospheric waves, quasi-geostrophic currents, SST fronts, and ageostrophic fronts (i.e. river plumes). All of these examples demonstrate a variety of factors important for understanding variations in whitecaps and wave energy dissipation.

The ability to observe whitecaps directly from space opens new opportunities to advance existing whitecap- and wave-breaking-retrieval algorithms based on passive microwave and SAR measurements. This also provides the possibility of correcting for the impact of wave breaking and foam on optical, infrared, active, and passive microwave measurements under moderate-to-high wind conditions.

Declaration of Competing Interest

The authors declare that they have no known competing financial interests or personal relationships that could have appeared to influence the work reported in this paper.

Acknowledgments

Vladimir Kudryavtsev acknowledges support of Russian Science Foundation project no. 17-77-30019 and state task 0763-2020-0005. Sergey Stanichny acknowledges support of RFBR project no. 19-05-00752. Kubryakov Arseny acknowledges support of state task 0555-2019-0001.

References

- Aleskerova, A.A., Kubryakov, A.A., Stanichny, S.V., Lishaev, P.N., Mizyuk, A.I., 2019. Cyanobacteria bloom in the Azov Sea according to Landsat data, *Izvestiya. Atmospheric and Oceanic Physics* 55 (9), 1416–1426.
- Anguelova, M.D., Webster, F., 2006. Whitecap coverage from satellite measurements: A first step toward modeling the variability of oceanic whitecaps. *Journal of Geophysical Research: Oceans* 111 (C3).
- Arduini, F., Jenkins, A.D., 2006. On the interaction of surface waves and upper ocean turbulence. *J. Phys. Oceanogr.* 36 (3), 551–557.
- Babanin, A.V., 2009. Breaking of ocean surface waves. *Acta Phys. Slovaca* 59 (4), 305–535.
- Banner, M.L., Babanin, A.V., Young, I.R., 2000. Breaking probability for dominant waves on the sea surface. *J. Phys. Oceanogr.* 30 (12), 3145–3160.
- Beal, R.C., Kudryavtsev, V.N., Thompson, D.R., Grodsky, S.A., Tilley, D.G., Dulov, V.A., Graber, H.C., 1997. The influence of the marine atmospheric boundary layer on ERS 1 synthetic aperture radar imagery of the Gulf stream. *Journal of Geophysical Research: Oceans* 102 (C3), 5799–5814.
- Becker, J.J., Sandwell, D.T., Smith, W.H.F., Braud, J., Binder, B., Depner, J., Ladner, R., 2009. Global bathymetry and elevation data at 30 arc seconds resolution: SRTM30 PLUS. *Mar. Geod.* 32 (4), 355–371.
- Bondur, V.G., Sharkov, E.A., 1982. Statistical properties of whitecaps on a rough sea. *Oceanology* 22 (3), 274–279.
- Boyce, F.M., 1975. Internal waves in the straits of Gibraltar. In: *Deep Sea Research and Oceanographic Abstracts*, vol. 22. Elsevier, pp. 597–610, 9.
- Brandt, P., Alpers, W., Backhaus, J.O., 1996. Study of the generation and propagation of internal waves in the strait of Gibraltar using a numerical model and synthetic aperture radar images of the European ERS 1 satellite. *Journal of Geophysical Research: Oceans* 101 (C6), 14237–14252.
- Brasseur, P., Beckers, J.M., Brankart, J.M., Schoenauen, R., 1996. Seasonal temperature and salinity fields in the Mediterranean Sea: climatological analyses of a historical data set. *Deep-Sea Res. I Oceanogr. Res. Pap.* 43 (2), 159–192.
- Brumer, S.E., Zappa, C.J., Brooks, I.M., Tamura, H., Brown, S.M., Blomquist, B.W., Cifuentes-Lorenzen, A., 2017. Whitecap coverage dependence on wind and wave statistics as observed during SO GasEx and HiWinGS. *J. Phys. Oceanogr.* 47 (9), 2211–2235.
- Callaghan, A.H., White, M., 2009. Automated processing of sea surface images for the determination of whitecap coverage. *J. Atmos. Ocean. Technol.* 26 (2), 383–394.
- Callaghan, A., de Leeuw, G., Cohen, L., O'Dowd, C.D., 2008. Relationship of oceanic whitecap coverage to wind speed and wind history. *Geophys. Res. Lett.* 35 (23).
- Callaghan, A.H., Stokes, M.D., Deane, G.B., 2014. The effect of water temperature on air entrainment, bubble plumes, and surface foam in a laboratory breaking-wave analog. *Journal of Geophysical Research: Oceans* 119 (11), 7463–7482.
- Cox, C., Munk, W., 1954. Measurement of the roughness of the sea surface from photographs of the sun's glitter. *JOSA* 44 (11), 838–850.
- D'Asaro, E.A., 2014. Turbulence in the upper-ocean mixed layer. *Annu. Rev. Mar. Sci.* 6, 101–115.
- De Leeuw, G., Andreas, E.L., Anguelova, M.D., Fairall, C.W., Lewis, E.R., O'Dowd, C., Schwartz, S.E., 2011. Production flux of sea spray aerosol. *Rev. Geophys.* 49 (2).
- De Loor, G., 1981. The observation of tidal patterns, currents, and bathymetry with SLAR imagery of the sea. *IEEE J. Ocean. Eng.* 6 (4), 124–129.
- Donelan, M.A., Dobson, F.W., Smith, S.D., Anderson, R.J., 1993. On the dependence of sea surface roughness on wave development. *J. Phys. Oceanogr.* 23, 2143–2149.
- Dulov, V.A., Kudryavtsev, V.N., 1990. Imagery of the inhomogeneities of currents on the ocean surface state. *Soviet journal of physical oceanography* 1 (5), 325–336.
- Dulov, V.A., Klyushnikov, S.I., Kudryavtsev, V.N., 1986. The effect of internal waves on the intensity of wind wave breaking. Field observation. *Morskoi Hydrofizicheskii Journal (English translation "Soviet Journal of Physical Oceanography")* 6, 14–21.
- Dulov, V.A., Klyushnikov, S.I., Kudryavtsev, V.N., Shulgin, O.V., Shcherbak, O.G., 1991. Reflection of large-scale inhomogeneities in the air-sea boundary layer on the intensity of surface wave breaking in the ocean. *Soviet journal of physical oceanography* 2 (4), 269–282.
- Dulov, V.A., Kudryavtsev, V.N., Bol'shakov, A.N., 2002. A field study of whitecap coverage and its modulations by energy containing surface waves. *Geophys. Monogr.* 127, 187–192.
- Fedorov, K.N., Ginsburg, A.I., 1989. Mushroom-like currents (vortex dipoles): one of the most widespread forms of non-stationary coherent motions in the ocean. In: *Elsevier Oceanography Series*, vol. 50. Elsevier, pp. 1–14.
- Frouin, R., Schwindling, M., Deschamps, P.Y., 1996. Spectral reflectance of sea foam in the visible and near-infrared: in situ measurements and remote sensing implications. *Journal of Geophysical Research: Oceans* 101 (C6), 14361–14371.
- Gemmrich, J.R., Banner, M.L., Garrett, C., 2008. Spectrally resolved energy dissipation rate and momentum flux of breaking waves. *J. Phys. Oceanogr.* 38 (6), 1296–1312.
- Goddijn-Murphy, L., Woolf, D.K., Callaghan, A.H., 2011. Parameterizations and algorithms for oceanic whitecap coverage. *J. Phys. Oceanogr.* 41 (4), 742–756.
- Gordon, H.R., Jacobs, M.M., 1977. Albedo of the ocean-atmosphere system: influence of sea foam. *Appl. Opt.* 16 (8), 2257–2260.
- Hansen, M.W., Kudryavtsev, V., Chapron, B., Brekke, C., Johannessen, J.A., 2016. Wave breaking in slicks: impacts on C-band quad-polarized SAR measurements. *IEEE Journal of Selected Topics in Applied Earth Observations and Remote Sensing* 9 (11), 4929–4940.
- Isern-Fontanet, J., Chapron, B., Lapeyre, G., Klein, P., 2006. Potential use of microwave sea surface temperatures for the estimation of ocean currents. *Geophys. Res. Lett.* 33 (24) <https://doi.org/10.1029/2006gl027801>.
- Kleiss, J.M., Melville, W.K., 2010. Observations of wave breaking kinematics in fetch-limited seas. *J. Phys. Oceanogr.* 40 (12), 2575–2604.
- KNMI, 2010. MetOp-A ASCAT Level 2 Ocean Surface Wind Vectors Optimized for Coastal Ocean. Ver. Operational/Near-Real-Time. PO.DAAC, CA, USA (Dataset accessed [YYYY-MM-DD]).
- Koepeke, P., 1984. Effective reflectance of oceanic whitecaps. *Appl. Opt.* 23 (11), 1816–1824.
- Koepeke, P., 1985. The reflectance factors of a rough ocean with foam—comment on 'remote sensing of the sea state using the 0.8–1.1 μm spectral band' by L. Wald and JM Monget. *Int. J. Remote Sens.* 6 (5), 787–797.
- Koepeke, P., 1986. Remote sensing signatures of whitecaps. In: *Oceanic Whitecaps*. Springer, Netherlands, pp. 251–260.
- Kokhanovsky, A.A., 2004. Spectral reflectance of whitecaps. *Journal of Geophysical Research: Oceans* 109 (C5).
- Korinenko, A.E., Malinovsky, V.V., Kudryavtsev, V.N., 2018. Experimental research of statistical characteristics of wind wave breaking. *Phys. Oceanogr.* 25 (6), 489.
- Kraan, G., Oost, W.A., Janssen, P.A.E.M., 1996. Wave energy dissipation by whitecaps. *J. Atmos. Ocean. Technol.* 13 (1), 262–267.
- Kudryavtsev, V.N., Grodsky, S.A., Dulov, V.A., Bol'shakov, A.N., 1995. Observations of wind waves in the Gulf stream frontal zone. *Journal of Geophysical Research: Oceans* 100 (C10), 20715–20727.
- Kudryavtsev, V., Grodsky, S., Dulov, V., Malinovsky, V., 1996. Observation of atmospheric boundary layer evolution above the Gulf stream frontal zone. *Bound.-Layer Meteorol.* 79, 18–82.
- Kudryavtsev, V., Akimov, D., Johannessen, J.A., Chapron, B., 2005. On radar imaging of current features. Part 1: Model and comparison with observations. *Journal of Geophysical Research* vol. 110, C07016. <https://doi.org/10.1029/2004JC002505>.
- Kudryavtsev, V., Dulov, V., Shrira, V., Malinovsky, V., 2008. On vertical structure of wind-driven sea surface currents. *J. Phys. Oceanogr.* 38 (10), 2121–2144.
- Kudryavtsev, V., Myasoedov, A., Chapron, B., Johannessen, J.A., Collard, F., 2012. Imaging mesoscale upper ocean dynamics using synthetic aperture radar and optical data. *J. Geophys. Res.* 117, C04029 <https://doi.org/10.1029/2011JC007492>.
- Kudryavtsev, V., Kozlov, I., Chapron, B., Johannessen, J.A., 2014. Quad-polarization SAR features of ocean currents. *J. Geophys. Res. Oceans* 119. <https://doi.org/10.1002/2014JC010173>.
- Kudryavtsev, V., Yurovskaya, M., Chapron, B., Collard, F., Donlon, C., 2017. Sun glitter imagery of Ocean Surface Waves. Part 2: Waves transformation on the Ocean Currents. *J. Geophys. Res. Oceans* 122. <https://doi.org/10.1002/2016JC024226>.
- Lim, Jae S., 1990. Two-Dimensional Signal and Image Processing. Prentice Hall, Englewood Cliffs, NJ, p. 548 (equations 9.26, 9.27, and 9.29).
- Liu, G., Perrie, W., Kudryavtsev, V., He, Y., Shen, H., Zhang, B., Hu, H., 2016. Radar imaging of intense nonlinear Ekman divergence. *Geophys. Res. Lett.* 43 (18), 9810–9818.
- Maul, G.A., Gordon, H.R., 1975. On the use of the earth resources technology satellite (LANDSAT-1) in optical oceanography. *Remote Sens. Environ.* 4, 95–128.
- Mellor, G., Blumberg, A., 2004. Wave breaking and ocean surface layer thermal response. *J. Phys. Oceanogr.* 34 (3), 693–698.
- Melville, W.K., Romero, L., Kleiss, J.M., 2005. Extreme wave events in the Gulf of Tehuantepec. *Rogue Waves*. In: *Proc. 14th MARCH 2017 R O M E R O E T A L. 631 'Aha Huli'ko'a Hawaiian Winter Workshop*. University of Hawai'i at Manoa, Honolulu, Hawaii, pp. 23–28.

- Mironov, A.S., Dulov, V.A., 2007. Detection of wave breaking using sea surface video records. *Meas. Sci. Technol.* 19 (1), 015405 <https://doi.org/10.1088/0957-0233/19/1/015405>.
- Monahan, E.C., 1971. Oceanic whitecaps. *J. Phys. Oceanogr.* 1 (2), 139–144.
- Monahan, E.C., Muircheartaigh, I., 1980. Optimal power-law description of oceanic whitecap coverage dependence on wind speed. *J. Phys. Oceanogr.* 10 (12), 2094–2099. [https://doi.org/10.1175/1520-0485\(1980\)0102.0.co;2](https://doi.org/10.1175/1520-0485(1980)0102.0.co;2).
- Monahan, E.C., O'Muircheartaigh, I.G., 1986. Whitecaps and the passive remote sensing of the ocean surface. *Int. J. Remote Sens.* 7 (5), 627–642.
- Moore, K.D., Voss, K.J., Gordon, H.R., 2000. Spectral reflectance of whitecaps: their contribution to water-leaving radiance. *Journal of Geophysical Research: Oceans* 105 (C3), 6493–6499.
- Ovchinnikov, I.M., Plakhin, E., 1976. *Hydrology of the Mediterranean Sea*. Gidrometeoizdat, Leningrad(USSR) 375.
- Phillips, O.M., 1985. Spectral and statistical properties of the equilibrium range in wind-generated gravity waves. *J. Fluid Mech.* 56, 505–531. <https://doi.org/10.1017/S0022112085002221>.
- Plant, W.J., 2012. Whitecaps in deep water. *Geophys. Res. Lett.* 39 (16).
- Qi, L., Hu, C., Mikelsons, K., Wang, M., Lance, V., Sun, S., Van der Zande, D., 2020. In search of floating algae and other organisms in global oceans and lakes. *Remote Sens. Environ.* 239, 111659.
- Quillen, Y., Yurovskaya, M., Chapron, B., Ardhuin, F., 2018. Storm waves focusing and steepening in the Agulhas current: satellite observations and modeling. *Remote Sens. Environ.* 216, 561–571. <https://doi.org/10.1016/j.rse.2018.07.020>.
- Randolph, K., Dierssen, H.M., Cifuentes-Lorenzen, A., Balch, W.M., Monahan, E.C., Zappa, C.J., Bowler, B., 2016. Novel methods for optically measuring whitecaps under natural wave breaking conditions in the Southern Ocean. *J. Atmos. Ocean. Technol.* 2016.
- Reuter, D., Richardson, C., Pellerano, F., Irons, J., Allen, R., Anderson, M., Tesfaye, Z., 2015. The thermal infrared sensor (TIRS) on Landsat 8: design overview and pre-launch characterization. *Remote Sens.* 7 (1), 1135–1153.
- Rienecker, M.M., Suarez, M.J., Gelaro, R., Todling, R., Bacmeister, J., Liu, E., Bloom, S., 2011. MERRA: NASA's modern-era retrospective analysis for research and applications. *Journal of Climate* 24 (14), 3624–3648.
- Romero, L., Lenain, L., Melville, W., 2017. Observations of surface wave-current interaction. *J. Phys. Oceanogr.* 47, 615–632. <https://doi.org/10.1175/JPO-D-16-0108.1>.
- Ross, D.B., Cardone, V., 1974. Observations of oceanic whitecaps and their relation to remote measurements of surface wind speed. *J. Geophys. Res.* 79 (3), 444–452.
- Salisbury, D.J., Anguelova, M.D., Brooks, I.M., 2013. On the variability of whitecap fraction using satellite-based observations. *Journal of Geophysical Research: Oceans* 118 (11), 6201–6222.
- Sarhan, T., Lafuente, J.G., Vargas, M., Vargas, J.M., Plaza, F., 2000. Upwelling mechanisms in the northwestern Alboran Sea. *J. Mar. Syst.* 23 (4), 317–331.
- Schott, J.R., Gerace, A., Woodcock, C.E., Wang, S., Zhu, Z., Wynne, R.H., Blinn, C.E., 2016. The impact of improved signal-to-noise ratios on algorithm performance: case studies for Landsat class instruments. *Remote Sens. Environ.* 185, 37–45.
- Selby, J.E.A., 1978. *Atmospheric Transmittance/Radiance: Computer Code LOWTRAN 4* (Vol. 78, No. 53). Air Force Geophysics Laboratory, Air Force Systems Command, United States Air Force.
- Stramska, M., Petelski, T., 2003. Observations of oceanic whitecaps in the north polar waters of the Atlantic. *Journal of Geophysical Research: Oceans* 108 (C3).
- Sutherland, P., Melville, W.K., 2013. Field measurements and scaling of ocean surface wave-breaking statistics. *Geophys. Res. Lett.* 40 (12), 3074–3079.
- Thomson, J., Gemmrich, J.R., Jessup, A.T., 2009. Energy dissipation and the spectral distribution of whitecaps. *Geophys. Res. Lett.* 36 (11).
- Thomson, J., Horner-Devine, A.R., Zippel, S., Rusch, C., Geyer, W., 2014. Wave breaking turbulence at the offshore front of the Columbia River plume. *Geophys. Res. Lett.* 41 (24), 8987–8993.
- Thorpe, S.A., Belloul, M.B., Hall, A.J., 1987. Internal waves and whitecaps. *Nature* 330 (6150), 740–742.
- Toffoli, A., McConochie, J., Ghantous, M., Loffredo, L., Babanin, A.V., 2012. The effect of wave-induced turbulence on the ocean mixed layer during tropical cyclones: field observations on the Australian north-west shelf. *Journal of Geophysical Research: Oceans* 117 (C11).
- Vlasenko, V., Sanchez Garrido, J.C., Stashchuk, N., Garcia Lafuente, J., Losada, M., 2009. Three-dimensional evolution of large-amplitude internal waves in the strait of Gibraltar. *J. Phys. Oceanogr.* 39 (9), 2230–2246.
- Whitlock, C.H., Bartlett, D.S., Gurganus, E.A., 1982. Sea foam reflectance and influence on optimum wavelength for remote sensing of ocean aerosols. *Geophys. Res. Lett.* 9 (6), 719–722.
- Wu, J., 1988. Variations of whitecap coverage with wind stress and water temperature. *Journal of Physical Oceanography* 18 (10), 1448–1453.
- Wu, L., Rutgersson, A., Sahlée, E., 2015. Upper-ocean mixing due to surface gravity waves. *Journal of Geophysical Research: Oceans* 120 (12), 8210–8228.
- Xu, Z., Zhou, W., Sun, Z., Yang, Y., Lin, J., Wang, G., Yang, Q., 2015. Estimating the augmented reflectance ratio of the ocean surface when whitecaps appear. *Remote Sens.* 7 (10), 13606–13625.
- Yu, P., Johannessen, J.A., Kudryavtsev, V., Zhong, X., Zhou, Y., 2016. Radar imaging of shallow water bathymetry: a case study in the Yangtze estuary. *Journal of Geophysical Research: Oceans* 121 (12), 8821–8839.
- Zhang, H., Lou, X., Li, Y., Shi, A., Li, D., Fu, B., 2015. Whitecap features induced by submarine sand waves in stereo optical imagery. *Journal of Geophysical Research: Oceans* 120 (9), 6225–6233.
- Zippel, S., Thomson, J., 2017. Surface wave breaking over sheared currents: observations from the mouth of the Columbia River. *J. Geophys. Res. Oceans*. Accepted Author Manuscript. <https://doi.org/10.1002/2016JC012498>.
- Zippel, S.F., Thomson, J., Farquharson, G., 2018. Turbulence from breaking surface waves at a river mouth. *J. Phys. Oceanogr.* 48, 435–453. <https://doi.org/10.1175/JPO-D-17-0122.1>.